

## Revisit the Oort constants measurement from *Gaia DR2* observations and simulations

SHUFAN XIA,<sup>1</sup> KARENS MASTERS,<sup>1</sup> AND ZHAO-YU LI<sup>2</sup>

<sup>1</sup>*Haverford College, Department of Physics and Astronomy*

<sup>2</sup>*Shanghai Jiaotong University, Department of Astronomy*

### ABSTRACT

The Oort constants parameterize stellar motion in the Milky Way Galaxy (MW). They describes the epicycle motions in radial, longitudinal, and latitude directions near the Sun. They prove Milky Way differential rotation and a flat MW rotation curve. An accurate determination of this set of constants helps us derive the MW rotation curve in the Sun’s immediate neighborhood. They can be used to find local Galactic parameters, such as orbit ellipticity, solar distance from the Galaxy’s center, etc. *Gaia* provides massive and exquisite data on parallax and proper motion of stars in the Milky Way. These data make it possible to determine the Oort constants in the solar vicinity with unprecedented accuracy. This work re-examines the influence of different sampling criteria on the stellar distance and latitude ranges in the Galactic coordinate used to derive the Oort constants based on *Gaia* DR2 data. We apply proper motion and line-of-sight velocity data from *Gaia* DR2 and compare the result with an idealized test particle simulation under an axisymmetric potential to determine the best stellar subsets for calculating the Oort constants. We found  $A =, B =, C =, K =$  from Gaia DR2 observational data, while  $A =, B =, C =, K =$  from our simulation.

### 1. INTRODUCTION

The simplest model of the Milky Way (MW) indicates that our galaxy is a flat circular disk, and stars move on perfectly circular orbits around the galactic center (GC). However, the structure and the dynamics of our galaxy is much more complicated. Our galaxy is a barred- spiral galaxy with non-axisymmetric and time-dependent perturbation to the potential. Due to perturbation in the MW potential, all stars have non-circular components to their orbital energy, so they move in elliptic and non-closed orbits (Binney & Merrifield 1998; Bovy 2017). The rotational kinematics of the MW is complicated to quantify. The Oort constants are a set of empirically

derived kinematic parameters  $A$ ,  $B$ ,  $C$ , and  $K$  that characterizes the local rotation properties in the Milky Way. They have been used extensively in the study of the rotational kinematics of our galaxy.

To help us keep track the different velocities in the following discussion, here I list the notation for velocity components used throughout this paper. In Galactocentric coordinate,  $v_{circ}$  or  $v_\phi$  is the circular velocity about the Galactic Center(GC);  $v_r$  is the radial velocity with respect to the GC;  $v_z$  is vertical velocity away from the Milky Way (MW) disk. In the Galactic coordinate (discussed further in Section 1.3 and Fig 2),  $v_{los}$  is the line of sight velocity as seen from the Sun;  $v_l$  is the velocity component perpendicular to the line of sight in the  $l$  direction; and  $v_b$  represents the velocity component perpendicular to the line of sight in the  $b$  direction.

### 1.1. The Milky Way Rotation Curve

The measurements of the rotation curves of galaxies, a function of circular rotational velocity,  $v_\phi$  about the galactic center over distance, has given us a proof for the existence of dark matters. From the flat but slightly declining rotation curve of the Milky Way, the mass components and their distribution in our Galaxy have been derived. Fig. 1 shows a recent measurement of the MW rotation curve (Eilers et al. 2019). The overall rotation curve comes from adding up the contributions from different components of mass - the central bulge, stellar disc, other stellar components and the dark matter halo (Olling & Merrifield 1998).

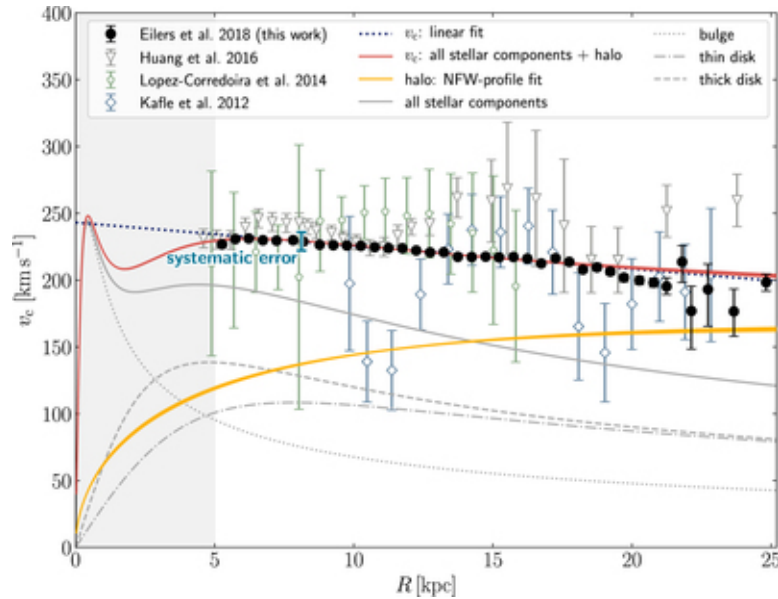


**Figure 1:** Recent measurements of the circular velocity curve of the Milky Way. The red curve is an approximate overall rotation curve (Eilers et al. 2019).

With Newtonian Mechanics, we can connect velocity, potential, and mass distribution (Binney & Merrifield 1998); therefore, kinematics is as a mass probe. The

implications of the rotation curve are multiple: it can be used to study kinematics, evolutionary histories of galaxies, and departures from Keplerian form due to dark matter (Sofue & Rubin 2001). However, measuring the Milky Way rotation curve is challenging because of the observation constraints from our location in the Milky Way. We are relatively close to the MW center and in one of the spiral arms of the Galaxy (Binney & Merrifield 1998). This means that our line of sight is blocked by dust, so we can not observe the other side of the Galaxy. The fact that we co-moving with the Galaxy also makes it challenging to determine relative motion. Therefore, measuring the whole rotation curve remains a challenging task.

Various objects and methods have been used to track the rotation curve. Determining distances is quite difficult because of the extinction from interstellar medium. For the inner region within the sun, the MW rotation curve has been determined via the tangent-point method using the line of sight velocity of HI or CO emission line measured from Doppler’s effect (Levine et al. 2008). Based on geometric and trigonometric derivations, this method is able determine distances and rotation velocity just from the radial velocities of gas clouds in a fixed direction but at different distances with respect to the observer. The rotation curve of the outer region beyond the Sun has been measured by other tracers, such as classical Cepheid (Joy 1939; Metzger et al. 1998; Mróz et al. 2019), RR lyrae stars (Wegg et al. 2019), and luminous red giant stars (Eilers et al. 2019). Both classical Cepheids and RR lyrae stars are better for determining rotation curve because they are intrinsically bright and their distance-period relationship makes distance measurement more reliable. (Metzger et al. 1998).

### 1.2. *Motivation*

While these methods require difficult observational measurements across a very large space, we can use the Oort constants to describe local rotational properties. Oort constants  $A$  and  $B$  (which are explained more in section 1.3 below) tell us the local rotational velocity around the galactic center and the local slope of the rotational curve (Binney & Merrifield 1998). The power of the Oort constants is that they are local parameters, but it enables us to test against different rotational models from their predicted rotation curves. This work looks at the Oort constants in the vicinity of our Sun. Accurate measurement of the Oort constants in this region will potentially help us determine the local rotation curve, galactic radius, and rotational velocity of the sun (Olling & Merrifield 1998), as well as the eccentricity of the solar orbit (Kuijken & Tremaine 1994; Metzger et al. 1998).

### 1.3. *Oort constants*

To study the local rotation near the Sun and the Oort constants, the following discussion is based on the Galactic coordinate. It is a spherical coordinate, with the Sun at its center and its plane parallel to the Milky Way midplane. Galactic longitude  $l$  is the counter-clockwise azimuthal measured from the Galactic center at

$l = 0$ , and the Galactic longitude,  $b$ , is the elevation angle (Fig.2). A nuance to this coordinate frame is that the Sun, in reality, does not stay in a rest frame called LSR which follows a perfect circular orbit. Its motion relative to the LSR is called peculiar motion (Binney & Merrifield 1998).

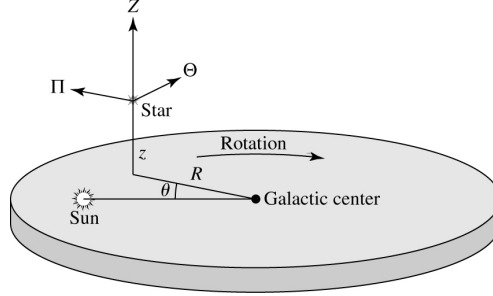


**Figure 2:** Galactic coordinate system. Figure adapted from Mihos unknown year.

Assuming the Milky Way has axisymmetric potential and stars are on circular orbits, Oort derived Oort constants  $A$  and  $B$  via radial velocities and tangential proper motions as a function of Galactic longitude  $l$  by Taylor-expanding the local velocity field to the first order about the local rotational center (Oort 1927). It is shown that the radial velocity and tangential velocity are proportional to  $\cos 2l$ ,  $\sin 2l$ :

$$v_r = A \sin 2l \quad \text{and} \quad v_\perp = d(A \cos 2l + B) \quad (1)$$

, where  $A = -\frac{1}{2} \left( \frac{dv_{\text{circ}}}{dR} - \frac{v_{\text{circ}}}{R} \right) \Big|_{R_\odot}$  and  $B = -\frac{1}{2} \left( \frac{dv_{\text{circ}}}{dR} + \frac{v_{\text{circ}}}{R} \right) \Big|_{R_\odot}$ .

In Oort's original measurement, he determined that near the Sun  $A \approx 19$  (km/s/kpc) and  $B \approx 24$  (km/s/kpc) (Oort 1927).  $A$  describes the local shearing, and  $B$  describes local vorticity. The result of a non-zero  $A$  suggests that stars near the Sun have varying rotation angular velocity, providing the first strong evidence that the Milky Way is rotating differentially. This result supported an earlier rotation model of the MW hypothesized by Lindblad. In Lindblad's hypothesis that the Galactic systems may be divided into subsystems (globular clusters). Each subsystem rotates around the Galactic center, and within each subsystem, objects rotate around a common axis but at different rotational speeds (Oort 1927).

The Oort constants were generalized to consider the Sun's peculiar motion with respect to nearby stars. It is derived analytically that the double sine (or cosine) trend is distinguishable from the pattern due to the Sun's peculiar motion about nearby stars. And two additional constants were introduced to the function of radial and tangential velocity against  $l$ , namely  $C$ , and  $K$  (Ogrodnikoff 1932). These four constants,  $A$ ,  $B$ ,  $C$ , and  $K$  describe transverse shear, vorticity, radial shear, and divergence in the local velocity field from Galactic rotation accordingly. The radial velocity,  $v_{los}$ , is:

$$v_{los} = d(K + C \cos 2l + A \sin 2l) \quad (2)$$

The proper motion in longitude and latitude direction,  $\mu_l$  and  $\mu_b$ , have the following dependence on  $2l$  (Olling & Dehnen 2003):

$$\mu_l = (A \cos 2l - C \sin 2l + B) \cos b + \varpi(u_0 \sin l - v_0 \cos l) \quad (3)$$

$$\mu_b = -(A \sin 2l + C \cos 2l + K) \sin b \cos b + \varpi[(u_0 \cos l + v_0 \sin l) \sin b - w_0 \cos b]. \quad (4)$$

In equations above, the single  $\sin$  and  $\cos$  terms represent the effect due to the sun's peculiar motion.

The local slope of the rotation curve,  $\frac{d\Theta}{dr}|_{R_\odot}$ , is given by  $-(A + B)$ , and rotational velocity,  $\Theta_\odot$  is  $R_\odot(A - B)$ . If the galaxy is not axis-symmetric,  $C$  and  $K$  are nonzero (Binney & Merrifield 1998, Ogrodnikoff 1932). In the Method section, I will present the full derivation of Oort constants. The Fourier series approximation approach has also been used to derive Oort constants. The Fourier coefficients of the 0 and 2 modes correspond to Oort Constants (Lin et al. 1978).

It must be emphasized that Oort constants can be extended to a set of functions depending on the distances from the Galactic center as we expand velocity fields about different distances. Typically, the Oort functions vary at a rate of a few  $km/s/kpc^2$  (Olling & Merrifield 1998). For distant stars in the disk, a higher order of the streaming velocity field equation must be taken into consideration (Siebert et al. 2011). The Oort constants in the first order of the streaming velocity field equation are restrained to the rotation in the solar vicinity because the higher-order contributions will become significant at large distances (Bovy 2017). Due to the contribution from interstellar gas in the MW which density varied non-monotonically with distance from the Galactic center, between  $0.9R_\odot$  and  $1.2R_\odot$ , the Oort functions  $A(R)$  and  $B(R)$  differ significantly from the general angular frequency dependence (Olling & Merrifield 1998). This suggests that when measuring the Oort constants, it is crucial to constrain the range of galactic distance.

#### 1.4. Measuring Oort constants

In order to measure the Oort constants based on Eq.??, we need to have locations and velocities of stars in the Galactic coordinate. From our vantage point on Earth, we can get radial velocities from the Doppler shift, and proper motions are measured optically by tracing the stars moving across the plane of the sky. The positions or the distances of stars are measured from parallax optically. Measurements of positions, radial velocities, and proper motions are then converted to the Galactic coordinate.

Many investigations have been conducted to attempt to use proper motion to determine the character of the non-uniformity of rotation and to measure the Oort constants. Fig.3 shows one example of measurement of Oort constants with proper motion. However, not all the results are in agreement (Kerr & Lynden-Bell 1986), which is mainly due to the absence of a complete proper motions catalog. A complete measurement of proper motion can give us stars distant enough that their random motions do not dominate their proper motions. It will also ensure sufficient sky coverage

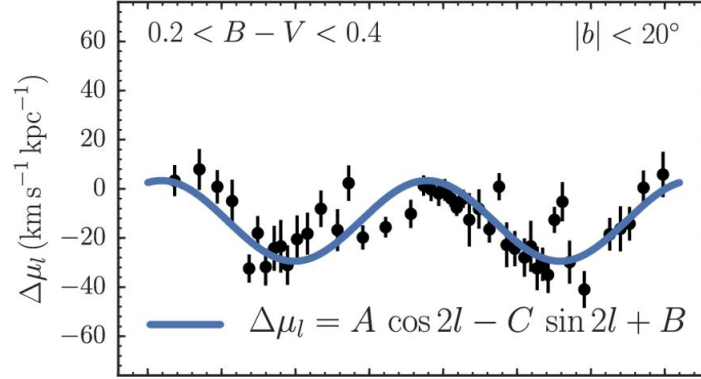


**Figure 3:** One example of historical measurement of Oort constants with observed proper motion in Galactic longitude: the value on  $y$ -axis is corrected for the solar motion based on Eq.???. The averages  $\mu_l(l)$  binned by  $l$  and their errors are plotted (Bovy 2017).

to allow the separation between the double sine curve of galactic proper motions from the single sine curve due to the solar motion in Eq.?? (Kerr & Lynden-Bell 1986). Although the observational precisions have been continuously developed, the values of  $A$  and  $B$  are still consistent with the values within uncertainties. However, for the values of  $C$  and  $K$ , it is another story (Li et al. 2019). Besides needing a complete proper motion catalog, three other factors complicate an accurate determination of values for the Oort constants.

First, the effect of non-axisymmetric potential associated with spiral or bar structure is not taken into account in Oort’s analysis. Observation data suggests the necessity of looking at a non-axisymmetric mode (Metzger et al. 1998). From the radial velocity of Cepheid, a significant zero-point offset (the Oort constant  $K$ ) in the radial velocities is suggested for a non-axisymmetric model. Metzger et al. (1998) also found a positive antisymmetric ellipticity component at R0. The deviations from the general axisymmetric velocity field, or the deviation from the Oort constants model specified by Eq 2, 3 and 4, could be used to study the non-circular motions in great detail and infer the mass associated with the spiral arms (Olling & Merrifield 1998).

Second, it is found that moderate strength in the spiral structure causes errors of order  $5 \text{ km/s/kpc}$  in  $A$  and  $B$  (Minchev & Quillen 2007). The spiral structure can be understood in the light of density waves where the spirals have concentrated stars. The streaming motion caused by density waves depending on the local spiral structure is difficult to determine (Lin et al. 1978). Further, the spiral structure raises the level of random motions in the Galactic disk (Sellwood & Carlberg 2014). Determination of other structural parameters to account for the effects from the Milky Way spirals must be made after a basic circular model in Section 1.3.

Third, the nonuniform distribution of parallax over longitudinal in conjunction with the solar peculiar motion contributes to significant 0 and 2 order terms deviated from



the first order Oort analysis (Olling & Dehnen 2003). This distribution of  $l$  may be due to intrinsic density nonuniformity and observational errors due to interstellar extinction. This systematic error has a contribution to the longitudinal proper motion  $\mu_l(l)$  indistinguishable from the effect of double  $\sin$  and  $\cos$  dependency. Olling & Dehnen (2003) suggested using the latitudinal proper motions  $\mu_l(l)$  of stars at low latitudes could correct for the errors from mode mixing.

### 1.5. Oort constants measurements based on *Gaia* data

In previous decades, the HIPPARCOS telescope had been used extensively in studying the MW kinematics, including deriving local Oort Constants and the rotation curve from classical cepheid (Feast & Whitelock 1997, Mignard 2000, Olling & Dehnen 2003). The *Gaia* mission (Gaia Collaboration et al. 2016a), since its launch by the European Space Agency in 2013, has collected astrometric parameters with unprecedented accuracy and multitude, aiming to build a three-dimensional map of our Galaxy. By the second release of *Gaia* data, we have the parallax and proper motions of over 1,600,000,000 stars (?). This also includes stars in higher latitude with significant latitude proper motion. Therefore, *Gaia*'s large set of astrometric measurements allows the first truly local precise measurement of the Oort constant and investigation of fine local kinematic features.

Two studies using *Gaia* DR1 and DR2 to calculate the Oorts Constant in solar vicinity yielded results in agreement (Bovy 2017; Li et al. 2019). The current values of the Oort constants based on DR2 is  $A = 15.1 \pm 0.1$ ,  $B = 13.4 \pm 0.1$ ,  $C = 2.7 \pm 0.1$ ,  $K = 1.7 \pm 0.2$ , all in the unit of km/s/kpc (Li et al. 2019). The slope of the rotation curve is determined from  $-(A + B)$  which is negative, thus confirming a slightly declining rotational curve in the solar vicinity. And significant non-zero  $C$  and  $K$  further indicate non-axisymmetric potential (Bovy 2017; Li et al. 2019). This suggests applying the axis-symmetric assumption of Oort analysis should be carefully examined. Both studies found the local Oort constants varied among different stellar populations based on their positions in the Hertzsprung-Russell Diagram. The result in Li et al. (2019) shows that the red giants deviate from the main-sequence stars in all four constants because they show more elliptical orbits and larger velocity dispersion. This finding is inconsistent with the suggestion in Olling & Dehnen (2003) that red giants are the “true” tracer of the Oort constants because they are old enough to be in equilibrium and distant enough to be unaffected by possible local anomalies. This disagreement suggests establishing an appropriate set of stars is critical to determine Oort constants accurately.

Previous work using HIPPARCOS and *Gaia* data to fit Oort constants used average proper motion binned by  $l$ , but fine features from each sample point in  $l$  vs proper motion are neglected, for example, Fig.3 (Bovy 2017, Li et al. 2019). Neither work used radial velocity information to determine the local Oort constants because the radial velocity measurement is only available for a fraction of the stars in the *Gaia*

data. However, a closer look at the radial velocity results and their deviation from the predicted theoretical model potentially entails significant information.

### 1.6. *Proposed research*

This work will focused on the Main Sequence (and Red Giant stars) from *Gaia* DR2. We used their latitudinal and longitudinal proper motions, as well as their radial velocity to determine the Solar local Oort constants.

As to measure Oort constants to higher precision and to understand the influence of sample selection on the final results, this work examined the conventional constraints on data sampling. In previous measurements of Oort constants (Olling & Dehnen 2003; Bovy 2017; Li et al. 2019), the sampling limit on parallax and latitude were explained qualitatively without justification. For example, Olling & Dehnen (2003) suggested, using the  $\mu_b$  of low latitudes stars, but both Bovy (2017) and Li et al. (2019) adopted the  $40^\circ < |b| < 50^\circ$  sampling criteria. Therefore, it is not clear, especially in the case of analyzing  $\mu_b$ , which subsets of stars in observation data should be used to derive the Oort constants and how using different subsets affects the final results.

We also used a simple 3D toy model of simulated test particle under the near circular orbital motion assumption to obtain a theoretical prediction of longitudinal and latitudinal proper motion,  $\mu_l$  and  $\mu_b$ , and radial velocity  $v_{los}$  as functions of Galactic longitude  $l$ . The model sampled 500,000 test particles moving under the MW potential specified by Bovy (2015). The goal of this model simulation and comparing it to observational data is twofold. First, it will allow us to find the range of parallax and Galactic latitude that give the best stellar subset(s) for Oort constants measurement. Second, it will help us to characterize the deviations in *Gaia*'s observational result from the expected model. The larger significance of this work is to provide a sample selection guidance for future Oort constants analysis.

In addition, to derive the Oort constants and their uncertainties, this work applied the Monte Carlo Markov Chain(MCMC) method to fit both observational results from *Gaia* and the simulation results of the toy model to Eq. 2, 3 and 4. Detail of the sample selection, MCMC fitting, and simulation are be included in the following sections. In the result section, we explored combining simulation and observational data together **have not done it at all**.

Finally, the recent third release of *Gaia* in December 2020 adds 200 million new samples to our database (?). This work looks forward to using this very new measurement to derive Oort constants. [I might just totally delete everything about EDR3, but mention it and the reason why I can't use it in future direction]

## 2. METHODS

### 2.1. *The Oort constants*

The Oort constants describe stellar streaming motions about the Sun in the Galactic coordinate, a right-handed coordinate where the direction from the Sun to the Milky Way (MW) galactic center is longitude  $l = 0$  and positive  $x$  (Fig 2). Consider a flat



2D Galactic disk under axisymmetric potential and the cold limit in which all stars move on closed orbits e.g. as defined in [Olling & Dehnen 2003](#), the position of a star on the disk is  $(x,y)$ , where  $(0,0)$  is at the Sun in the Galactic coordinate. The velocity field  $\langle v \rangle$  gives the average velocity at each point on the disk. In solar vicinity, the velocity at  $(x,y)$  may be expanded in a Taylor series about the Sun:

$$\langle v \rangle|_{(x,y)} = \langle v \rangle|_{(0,0)} + \begin{pmatrix} v_{xx} & v_{xy} \\ v_{yx} & v_{yy} \end{pmatrix} \bigg|_{(0,0)} \begin{pmatrix} x \\ y \end{pmatrix} \quad (5)$$

where  $\begin{pmatrix} v_{xx} & v_{xy} \\ v_{yx} & v_{yy} \end{pmatrix} = \begin{pmatrix} K + C & A - B \\ A + B & K - C \end{pmatrix} \bigg|_{(0,0)}$ , where A, B, C and K are the Oort constants. The relative velocity of the star as observed from the Sun is given by

$$\delta \langle v \rangle|_{(x,y)} = \langle v \rangle|_{(x,y)} - \langle v \rangle|_{(0,0)} \quad (6)$$

. The line of sight velocity is the component of  $\delta \langle v \rangle$  parallel to the galactic distance  $d$ :

$$v_{los} = \hat{d} \cdot \delta \langle v \rangle = \frac{(x,y)}{d} \cdot \begin{pmatrix} K + C & A - B \\ A + B & K - C \end{pmatrix} \bigg|_{(0,0)} \begin{pmatrix} x \\ y \end{pmatrix} \quad (7)$$

. After taking the dot product and applying trigonometric relations, we have

$$v_{los} = d[K + A \sin(2l) + C \cos(2l)] \quad (8)$$

Similarly, the longitudinal proper motion, perpendicular component of the relative velocity over  $d$ , is:

$$\mu_{\perp} = \frac{1}{d}(\hat{d} \times \delta \langle v \rangle) = B + A \cos(2l) - C \sin(2l) \quad (9)$$

In the model of local rotation, instead of the actual Sun position because the Sun moves in a non-circular orbit about the GC, to account for this non-circular deviation, we define a hypothetical reference point, Local Standard of Rest (LSR), as the reference frame. The LSR is at the same position of the Sun and moves on a circular orbit  $220 \text{ km s}^{-1}$ , and the relative motions of the Sun with respect to this LSR is described by peculiar motion,  $(u_0, v_0, w_0)$ , velocity in radial, tangential and vertical direction respectively. After correcting the solar peculiar motion, Eq 8 and 9 turn to:

$$v_{los} = d[K + A \sin(2l) + C \cos(2l)] - u_0 \cos(l) - v_0 \sin(l) \quad (10)$$

$$\mu_l = B + A \cos(2l) - C \sin(2l) + \frac{1}{d}[u_0 \sin(l) - v_0 \cos(l)] \quad (11)$$

where the  $\cos b$  term in Eq 11 accounts for the projection of distance onto the Galactic plane in a 3D MW disk. If the vertical velocity  $v_z$  of the star is non-zero, the latitudinal relative velocity at  $(l, b, d)$  is given by  $v_z(\cos b) - v_r \sin(b)$  ([Olling & Dehnen 2003](#)), and the latitudinal proper motion is:

$$\mu_b = -(A \sin 2l + C \cos 2l + K) \sin b \cos b + \varpi[(u_0 \cos l + v_0 \sin l) \sin b - w_0 \cos b] \quad (12)$$

Eq 10, 11 and 12 together give a model to determine Oort constants from observational data, and the full model parameter is  $\theta(A, B, C, K, u_0, v_0, w_0)$ .

## 2.2. Sample selection and stellar parameter estimation

The Gaia (Global Astrometric Interferometer for Astrophysics) mission of the European Space Agency (ESA) surveys about one billion stars in the MW photometrically and spectroscopically to make the most accurate three-dimensional map of the Galaxy. Gaia samples kinematic tracers dimmer to a magnitude limit of at least  $G = 20$  mag in the MW disks, bulge, and halo. The instrument package of Gaia spacecraft comprises two identical optical telescopes/imaging systems, a radial velocity spectrometer, and blue and red photometers. The unfiltered, white-light photometric  $G$  band of the optical telescope covers 330–1050 nm (Gaia Collaboration et al. 2016). The parallax uncertainties are 0.5 mas at  $G = 20$ . The uncertainties in proper motion are 0.5 mas yr<sup>-1</sup> at  $G = 20$  (Gaia Collaboration et al. 2018).

The radial-velocity spectrometer obtains radial velocities by measuring the Doppler-shift in the lines of stellar spectra. DR2 has the radial velocity of more than 7.2 million stars with a mean  $G = 4 - 13$  mag and an effective temperature in the range 3550 to 6900 K. The overall precision of the radial velocities range from 200-300 m s<sup>-1</sup> to 1.2-3.5 km s<sup>-1</sup> (Gaia Collaboration et al. 2016).

Astrophysical parameters such as effective temperature, surface gravity, metallicity, and extinction are derived from the BP and RP data measured by the blue and red photometers over the wavelength ranges 330–680 nm and 630–1050 nm (Gaia Collaboration et al. 2016).

In December 2020, ESA released the third intermediate *Gaia* data (EDR3). This version of release catalogs the positions and proper motions, and other photometric data of 1,811,709,771 stars, 1,692,919,135 entries of which are updated from DR2. The radial velocity data in EDR3 is added from the 7.2 million data in DR2 after deleting 4000 wrong entries. Furthermore, EDR3 deleted several entries from DR2, including color excess, extinction, and tag for marking variable star samples (Gaia Collaboration et al. 2020). I used the TAP service from TOPCAT (Tool for Operations on Catalogues And Tables) to access, process, and select the DR2 and EDR3 data (Taylor 2005).

Since the first-order Taylor approximation in Eq 5 is only appropriate for Solar vicinity, the stellar samples are limited to the region within 500 pc (2mas) from the Sun. And restricting  $\text{parallax/error} \geq 10$  will avoid additional bias from inverting the parallax to estimate distance (Luri et al. 2018). The uncertainties in the BP and RP fluxes are restrained to less than 10% in making an HR diagram and selecting the main sequence samples. Potential duplicate sources are also removed.

The main sequence stars are selected by drawing on the H-R diagram in TOPCAT. Extinction  $A_G$  and color excess  $E(B-V)$  must be considered when making an H-R diagram to reflect the properties of stars accurately. However, spectroscopic data, such

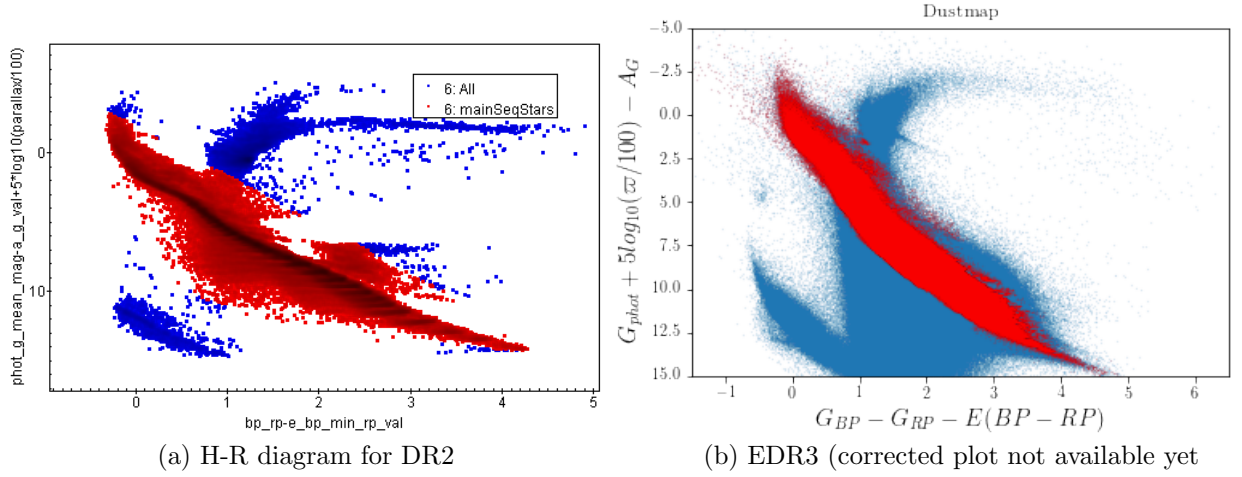


**Figure 4:** the H-R diagram and Main sequence star samples in DR2 and EDR3 after parallax, extinction and color excess correction.

as radial velocity, extinction, and color excess are not yet available for the 100 million newly added stars in EDR3. These data are expected to be published in DR3 in the first half of 2022 (Gaia Collaboration et al. 2020). Instead of doing a cross-match with DR2 samples,  $E(B - V)$  in EDR3 are calculated from the DUSTMAP python library because the new spectroscopic measurements in EDR3 and DR3 use different blue and red photometers than those in DR2. DUSTMAP gives a 3D map of interstellar dust reddening probabilistically based on broadband photometric measurement from Pan-STARRS 1, 2MASS, and Gaia parallaxes (Green 2018). Each  $(l, b, d)$  corresponds to a color excess value in the default *bayestar17* module in DUSTMAP, which I multiplied with  $R_v = 3.1$  to get the extinction. For EDR3, the position data is first retrieved from TOPCAT, then used to find  $E(B - V)$  and  $A_G$  in python. The original data along with calculated  $E(B - V)$  and  $A_G$  are used to plot H-R in TOPCAT again, and I drew out the main sequence samples on this diagram. Fig 4 shows the H-R diagram and Main sequence star samples in DR2 and EDR3 after applying parallax, extinction and color excess corrections. For DR2, color excess and extinction values used are from Gaia observation.

Because the local Oort constants varied among different stellar populations based on their color, thus their collective kinematic properties, I grouped the main sequence stars into six color groups on the H-R diagram based on color according to the criteria of Li et al. 2019. The rotational kinematics properties and the corresponding Oort constants for color group are analyzed individually. Table 1 shows the number of stars in each stellar group, as well as the corresponding numbers in DR2.

The proper motions and radial velocity entries in Gaia are measured in the equatorial coordinates system (ICRS), i.e. right ascension ( $\alpha$ ) and declination ( $\delta$ ) proper motions,  $\mu_\alpha$  and  $\mu_\delta$ . I used the SkyCoord class in *astropy* (Astropy Collaboration et al. 2018) to transform proper motions and available radial velocity from ICRS to

$BP\_RP - e\_bp\_min\_rp\_val$	$< 0.8$	$0.8 - < 1.2$	$1.2 - 1.6$	$1.6 - < 2.0$	$2.0 - 2.4$	$\geq 2.4$
DR2	978428	1591020	1284402	1086626	865742	351820
EDR3	649939	792940	1304201	2173292	347488	9356

**Table 1:** Number of main sequence stars fall into each color group for DR2 and EDR3. (will update these counts)

the Galactic coordinate. The units of proper motion are also converted from mas yr<sup>-1</sup> to km s<sup>-1</sup> kpc<sup>-1</sup> by multiplying 4.74047.

### 2.3. Estimating the parameters and their corresponding uncertainties:

#### Monte-Carlo-Markov-Chain

The parameters in the model of Eq 10, 11 and 12 consist of the four Oort constants and three peculiar velocity components. For such high-dimensional parameter space, I used the Monte Carlo Markov Chain (MCMC) method to determine the value and uncertainty of each parameter. The MCMC method combines our prior knowledge about the model and evidence from the data to obtain a posterior distribution of the model parameter  $\theta$ , in this case,  $\theta(A, B, C, K, u_0, v_0, w_0)$ . When fitting Gaia observational data in MCMC, the proper motions in longitude and latitude direction are considered together, but radial velocity is separated because this data is incomplete. The logarithmic likelihood function used is defined as:

$$\ln \mathcal{L}_\infty = - \sum_i \left( \frac{(med(\mu_l)_i - y_{1i})^2}{\sigma_{med(\mu_l)}^2 + error_{med(\mu_l)}^2} - \ln \frac{2\pi}{\sigma_{med(\mu_l)}^2 + error_{med(\mu_l)}^2} \right. \\ \left. + \frac{(med(\mu_b)_i - y_{2i})^2}{\sigma_{med(\mu_b)}^2 + error_{med(\mu_b)}^2} - \ln \frac{2\pi}{\sigma_{med(\mu_b)}^2 + error_{med(\mu_b)}^2} \right) \quad (13)$$

where  $\sigma_{med(\mu_l)}$  and  $\sigma_{med(\mu_b)}$  are the Gaussian scatter for the distribution of binned medians,  $error_{med(\mu_l)}^2$  and  $error_{med(\mu_b)}^2$  are the standard deviations within each bin, and  $y_1$  and  $y_2$  are given by Eq 11 and 12.

The prior distribution of  $\theta$  is defined as following:

$$P(\theta) = \begin{cases} 0 & \text{if } 10 < A < 20, \quad -15 < B < -5, \quad -5 < C < 5, \text{ and } -5 < K < 5 \\ -\infty & \text{if } A, B, C \text{ and } K \text{ are not within the range above} \end{cases} \quad (14)$$

And the overall logarithmic posterior probability is:

$$\ln P(\theta|y) = \begin{cases} \ln L & \text{if } P(\theta) = 0 \\ 0 & \text{if } P(\theta) = -\infty \end{cases} \quad (15)$$

I employed the *emcee* (Foreman-Mackey et al. 2013) python package and posterior probability Eq 15 to sample and update Markov Chains in MCMC.

## 2.4. Test particle simulation

To know what behaviors are expected from the theoretical Oort constants model, and thus understand how the actual MW deviates from the theoretical model, we constructed a toy model simulation, treating stars as test particles in a fixed MW potential and assuming all the model constraints of the Oort constants and the Sun stays on a circular orbit. I sampled 20,000 of test particles from *galpy*'s quasi-isothermal distribution function to represent a thin 3D Milky Way galactic disk. The distance from the Sun to the Galactic center and the circular velocity at the solar radius are set to  $R_0 = 8$  kpc and  $v_0 = 220$  km/s respectively. The horizontal scale of the disc is 0.4 kpc, and the radial velocity dispersion is chosen as 10km/s. This distribution function provides planar and vertical profiles of the thin disc with analytic function dependent on the action integrals in an integrable, axisymmetric Hamiltonian (Binney 2010). The potential in the Hamiltonian is specified by MWPotential2014 (Bovy 2015).

MWPotential2014 serves as a simple and accurate model for the MW potential from fitting to a large variety of dynamical data. This potential model consists of a bulge potential with a power law exponent of 1.8 and a cut-off radius of 1.9kpc (PowerSphericalPotentialwCutoff), a disk potential specified by MiyamotoNagaiPotential, and a dark-matter halo described by an NFWPotential (Bovy 2015). Fig 5 shows the spatial distribution of test particles sampled from the quasi-isothermal distribution function.

Besides, because we set the peculiar motion of the Sun to 0, the coordinate and velocity of LSR and the Sun are equivalent. All particles undergo 10Gyr of orbit integration under the potential specified by MWPotential2014 to reach equilibrium. The positions and velocities after 10Gyr are then used to calculate  $\mu_l$  and  $\mu_b$ , as well as  $v_{los}$ . Similar to the procedure of analyzing Gaia data, I binned the simulation data and used the binned medians to fit the three equations in Eq 10, 11 and 12, except  $u_0$ ,  $v_0$ , and  $w_0$  are set to 0. The log likelihood for MCMC is defined as:

$$\ln \mathcal{L}_2 = \ln \mathcal{L}_1 - \sum_i \left( \frac{(med(v_{los})_i - y_3)^2}{\sigma_{med(v_{los})}^2 + error_{med(v_{los})}^2} - \ln \frac{2\pi}{\sigma_{med(v_{los})}^2 + error_{med(v_{los})}^2} \right) \quad (16)$$

where  $\ln \mathcal{L}_1$  is from Eq 13,  $\sigma_{med(v_{los})}$  is the Gaussian scatter for the distribution of binned medians of  $v_{los}$ ,  $error_{med(v_{los})}$  is the standard deviations within each bin of  $v_{los}$ , and  $y_3$  is given by Eq 10.

## 3. RESULTS

### 3.1. Simulation: The effect of sampling criteria on $\mu_l$ , $v_{los}$ , $\mu_b$

From the simulation with 500,000 stars (test particles) described in above (Section 2.4), we examined the effect of different sampling criteria on the resulting proper motions ( $\mu_l$  and  $\mu_b$ ) and the line-of-sight velocity ( $v_{los}$ ) dependency on  $l$ . Fig 5a

displays the distribution of all the particles in 16 kpc from the GC and  $\pm 4$  kpc in the vertical direction. This disc looks thicker despite the scale height in the quasi-isothermal distribution function (Section 2.4) was set to 0.4 kpc because the tail of exponential distribution is evident when sample size is large. Out of the 500,000 particles, most reside on the other side of the Sun, far away from the Sun. In Fig 5b, we showed those stars within  $d = 4$  kpc from the Sun. we replicated the Sun's position at another symmetric three positions (0, 8kpc, 0), (-8kpc, 0, 0) and (0, -8kpc, 0) in the Cartesian form of the Galactocentric coordinate. This increase the number of stars nearby the Sun(s) so and gave us more available simulation results to analyze and derive the Oort constants.

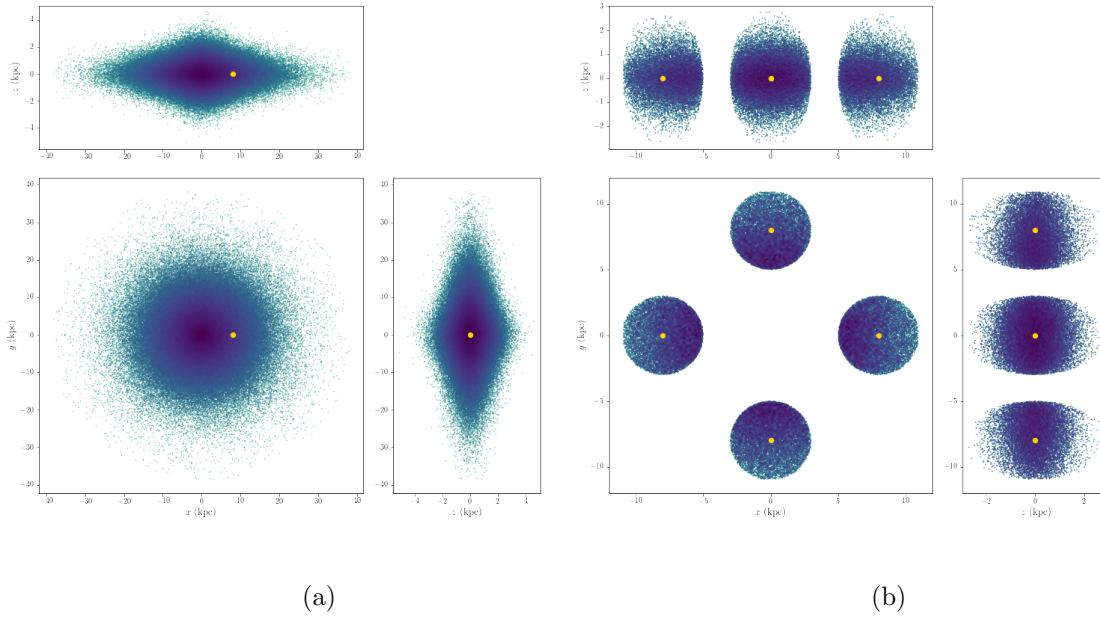


**Figure 5:** (a) The distribution of the 500,000 test particles (stars) sampled from quasi-isothermal distribution function for the Milky Way. (b) The distribution of simulated stars within  $d = 4$  kpc from the Sun, where We replicated the Sun at four different positions to increase effective samples near the Sun. Darker color correspond to higher density

### 3.1.1. $\mu_l$ and $v_{los}$

In Fig 6, we present the result of  $\mu_l$  vs  $l$  under three sample filtering criteria on the galactic distance  $d$  for stars that approximately lie on the ME mid plane ( $|b| < 20^\circ$ ). Proper motions after correcting the contribution in latitudinal direction ( $\cos b$ ) are mostly negative across  $l = 0^\circ$  to  $360^\circ$ , indicating that stars move in the decreasing  $l$  direction. Fig 6 also shows  $\mu_l$  has slightly positive value at  $l = 0^\circ, 180^\circ$ , and  $360^\circ$ .  $\mu_l$



is most negative and has larger variation among stars with the same  $l$  value at  $l = 90^\circ$  and  $270^\circ$  compared to the stars at  $l = 0^\circ, 180^\circ$ , or  $360^\circ$ .

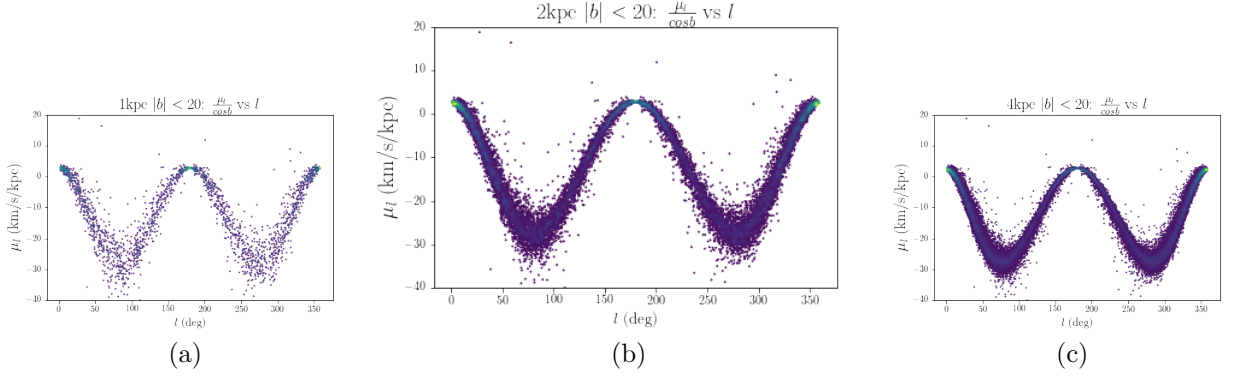


**Figure 6:** The distribution of  $\mu_l / \cos b$  over  $l$  for stars with  $|b| \leq 20$  and (a)  $d \leq 1\text{kpc}$ , (b)  $d \leq 2\text{kpc}$ , and (c)  $d \leq 4\text{kpc}$

In Fig 22d, we see for stars with  $d < 2\text{kpc}$  and  $|b| < 20$ ,  $v_{los}$  after divided by  $d$  traces a single double sinusoidal function as expected from Eq10.  $v_{los}$  is 0 at  $l = 0^\circ, 90^\circ, 180^\circ, 270^\circ$ . Positive  $v_{los}$  between  $l = 0^\circ$  to  $90^\circ$  and  $l = 180^\circ$  and  $270^\circ$  suggests stars move away from the Sun, while they approach the Sun in the line of sight direction between  $l = 90^\circ$  and  $180^\circ, 270^\circ$  and  $360^\circ$ . We show the comparison of  $v_{los}/d$  vs  $l$  under three sample filtering criteria on  $d$  while keeping  $|b| < 20$  in Fig 7a and 7c.

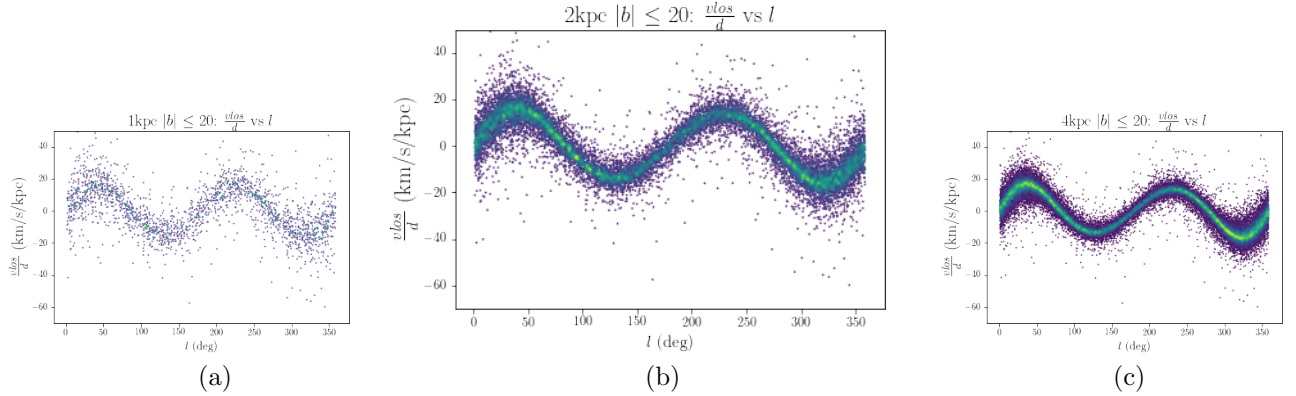


**Figure 7:** The distribution of  $v_{los}/d$  over  $l$  for stars with  $|b| \leq 20$  and (a)  $d \leq 1\text{kpc}$ , (b)  $d \leq 2\text{kpc}$ , and (c)  $d \leq 4\text{kpc}$

In Fig 8, we use a 2D velocity vector analysis of stars nearby the Sun at different longitude  $l$  to illustrate the variation of  $\mu_l$  and  $v_{los}$ . We assume these stars are all in circular orbits with radius  $R_{star}$  around the GC. When  $R_{star}$  is close to  $R_\odot$ ,  $v_\phi$  is approximately in the same direction. At  $l = 0^\circ$  and  $180^\circ$ ,  $v_\phi$  is in the line of LSR,

and  $v_\phi$  is perpendicular to the line of sight. As a result,  $v_{los} = 0$  and  $v_l = v_\phi - v_{\phi\odot}$ . According to the rotation velocity curve in (Fig 1), the radial profile of  $v_\phi$  is flat while slightly declining at  $R = R_\odot$ . As a result, the star moves in the direction of increasing  $l$ , giving  $\mu_l$  a small positive value at  $l = 0^\circ$  in the inner side of the MW disk. At  $l=180$ , because  $v_\phi$  is smaller than  $v_{\phi\odot}$ , the star lags behind the Sun, moving in the direction of increasing  $l$  (Fig ??, and  $\mu_l$  is expected to be positive.

At  $l = 90^\circ$  and  $270^\circ$ , stars are approximately in the same circular orbits as the Sun. They are essentially moving at the same speed as the sun along the line of sight, thus  $v_{los} = 0^\circ$ . However, to examine their proper motion, we need to zoom in closer to show that  $v_{phi}$  varies slightly in their direction. And Fig 14 shows the perpendicular component  $v_l$  points in the decreasing  $l$  direction at both  $l = 90^\circ$  and  $270^\circ$ .

At  $l = 45^\circ$ ,  $225^\circ$ ,  $l = 135^\circ$  and  $315^\circ$ , the orange vectors in Fig 8a and 8b indicate the relative velocity in the line-of-sight and tangential  $l$  direction after comparing to the velocity of the Sun in each direction respectively. We show that at  $l = 45^\circ$ ,  $v_{los} > 0$  and  $v_l < 0$ ;  $l = 45^\circ$ ,  $v_{los} < 0$  and  $v_l < 0$ ;  $l = 135^\circ$ ,  $v_{los} > 0$  and  $v_l < 0$ ;  $l = 225^\circ$ ,  $v_{los} > 0$  and  $v_l < 0$ ;  $l = 315^\circ$ ,  $v_{los} > 0$  and  $v_l < 0$ .

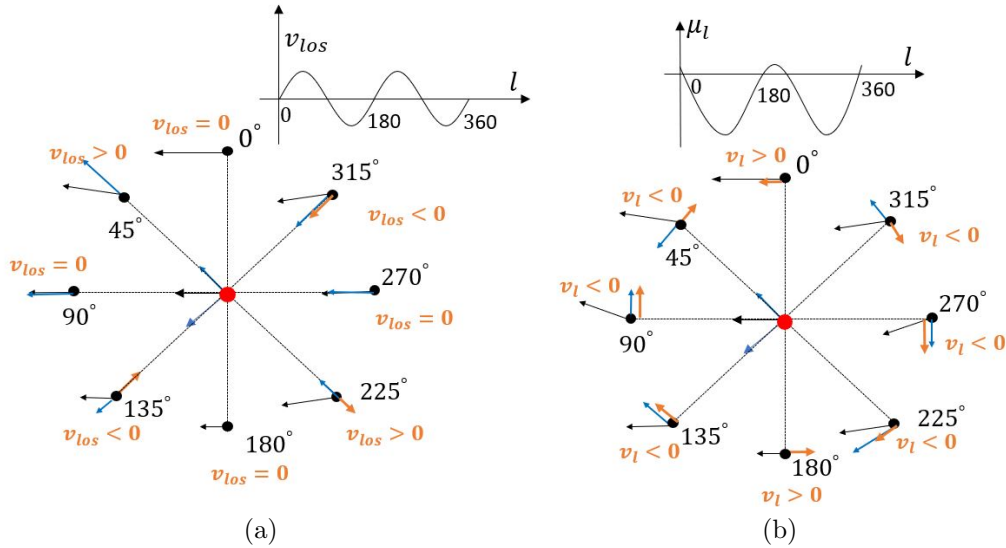


**Figure 8:** The variation in the radial velocity and transverse velocity among different Galactic longitude due to differential rotation of the Milky Way. The black arrows represent the velocity vector of  $v_\phi$ . The blue vectors represent the components in 8a the line of sight direction and 8b the longitudinal direction. The orange arrows are the relative velocity vectors in the two directions after taking the circular motion of the Sun into account.

### 3.1.2. The effect of $d$ on the longitudinal profile of $\mu_l$ and $v_{los}$

In Fig 6 and Fig 7, the number of samples selected drops from 51196 to 16741 and to 2310 as the galactic distance cut-off decreases from 4kpc, to 2kpc, and to 1kpc.

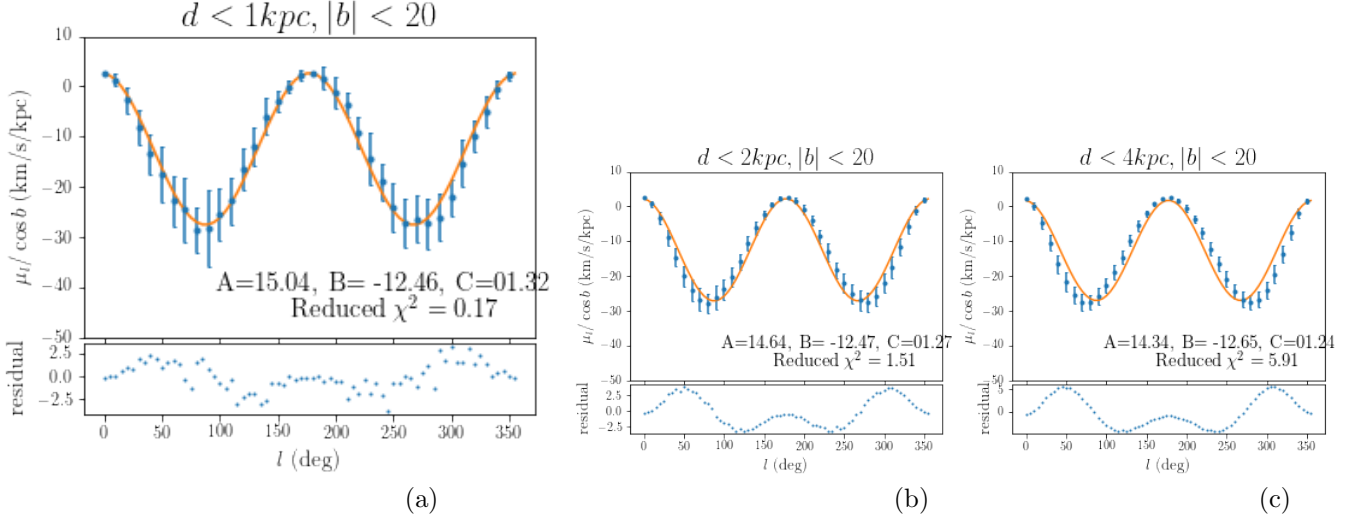


**Figure 9:** The function of binned median  $\mu_l / \cos b$  over  $l$  for stars with  $|b| \leq 20^\circ$  and (a)  $d \leq 1\text{kpc}$ , (b)  $d \leq 2\text{kpc}$ , and (c)  $d \leq 4\text{kpc}$ . The orange continuous curves come from fitting the binned median data to Eq 11 with maximum likelihood approximation. Only 36 out of 72 binned medians are plotted.

Despite the dispersion of  $\mu_l / \cos b$  and  $v_{los}/d$  are unaffected by the distance cut-off chosen in Fig. 6, the binned median values reveal some differences. In Fig 9, all the scatter data of Fig 6 are grouped into bins with a width of  $l = 5^\circ$ , and the median of  $\mu_l$  in each bin is plotted against  $l$ . The error bars are the standard deviations of the corresponding bins. For the simulated stars within 4kpc, there are significant deviations from the double cosine function (Fig 9c). This result suggests that 4kpc is too large for the first-order Taylor expansion around the Sun in Eq 5. The stars within 2kpc yield a reduced  $\chi^2$  closest to 1. However, including higher-order terms, such as  $\sin(3l)$ ,  $\cos(3l)$ , etc would fit these simulated data points more accurately. (Is this due to using a larger region for Taylor expansion or physical reason? Need to expand here) The proper motions of stars within 1kpc from the sun trace the double sinusoidal function best compared to 2kpc and 4kpc, and the residuals are also smallest for this group. However, this galactic distance cut-off only yielded 2310 out of 500,000 that meet this filtering criteria. The standard deviation within each bin is larger because a smaller sample size is more subjective to the difference between individual values and the medians.

Similarly, the binned  $v_{los}$  median of stars within  $d < 1\text{kpc}$  and  $|b| < 20^\circ$  give  $v_{los}/d$  vs  $l$  closet to the function in Eq10 compared to the stars within 4kpc and 2kpc. The reduced  $\chi^2$  values calculated for all the fitting above do not give informative measurements on the goodness of the fit. Reduced  $\chi^2$  being much larger than 1 suggests errors are underestimated, and overestimated for Reduced  $\chi^2$  being much smaller than 1. However for our simulated data, the errors come from standard deviation within each bin. Instead, we look at the range and distribution in the

residual vs  $l$  profile to decide if the fit is satisfactory. For both  $\mu_l/\cos b$  and  $v_{los}/d$ , the residual profiles for  $d < 1$  kpc have the smallest ranges. Moreover, for the fittings of  $d < 2$  kpc or  $d < 4$  kpc samples, the residual distribution is not uniform above or below 0 but exhibits a clear dependency on  $l$ , while when  $d < 1$  kpc, residual distributed randomly above and below 0. The dependency of residuals on  $l$  seems worthy for further investigation in future work.

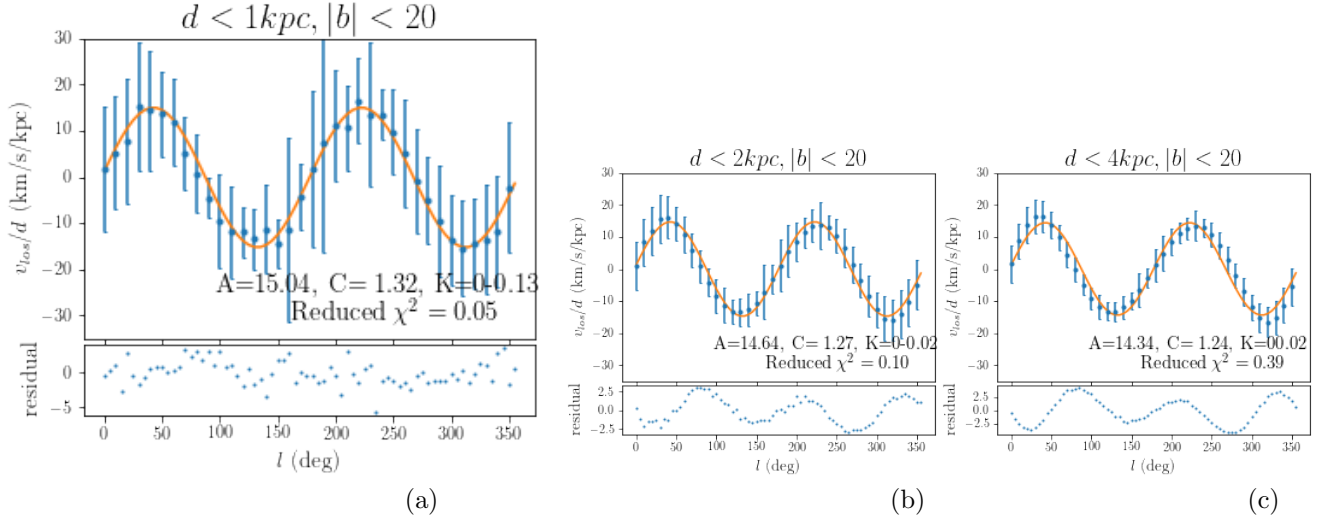


**Figure 10:** The function of binned median  $v_{los}/d$  over  $l$  for stars with  $|b| \leq 20^\circ$  and (a)  $d \leq 1$  kpc, (b)  $d \leq 2$  kpc, and (c)  $d \leq 4$  kpc. The orange continuous curves come from fitting the binned median data to Eq 10 with maximum likelihood approximation. Only 36 out of 72 binned medians are plotted.

### 3.1.3. The effect of $b$ on the longitudinal profiles of $\mu_l$ and $v_{los}$

In Fig 11, we compared binned  $\mu_l$  median vs  $l$  of stars at  $d < 2$  kpc from the Sun but at different latitude ranges,  $|b| < 20^\circ$ ,  $30^\circ < |b| < 50^\circ$  and  $60^\circ < |b| < 80^\circ$ . The scatter in the  $\mu_l$  around the central double sinusoidal line increases for higher latitude regions as suggested by the error bars on the binned median data. When  $|b| \leq 20^\circ$ , stars are considered close to the MW mid-plane, thus are most suitable to fit the model in Eq 11. For  $30^\circ \leq |b| \leq 50^\circ$ , the scattered data deviate from the double cosine function considerably. And for  $60^\circ \leq |b| \leq 80^\circ$ , not only the spread in the scattered data is the largest, the binned medians deviate from the fitted double cosine function more significantly according to the residual vs  $l$  panel in Fig 11.

Likewise, in Fig 12, the spread in the  $v_{los}/d$  of the stars within 2kpc from the Sun but at a higher latitude  $b$  is larger. Comparing the residual profiles in the lower panels, we see the range of residuals is the smallest for the group closet to the MW mid-plane. This suggests the deviation of binned  $v_{los}/d$  median from the predicted double sine function is smallest for stars at  $|b| < 20^\circ$  and largest at  $60^\circ < |b| < 80^\circ$ . With a larger  $b$  value, we move away from the Milky Way (MW) disk, and the orbits get less

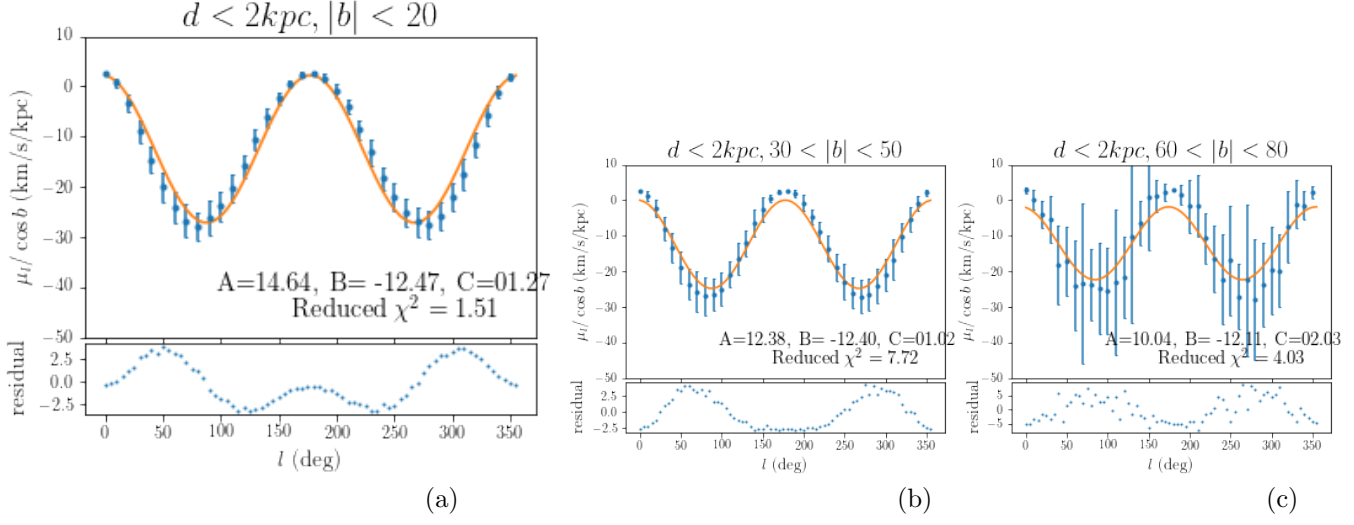


**Figure 11:** The function of binned median  $\mu_l / \cos b$  over  $l$  for stars with  $d < 2\text{kpc}$  and (a)  $|b| \leq 20^\circ$ , (b)  $30^\circ < |b| < 50^\circ$ , and (c)  $60^\circ < |b| < 80^\circ$ .

circular. MW potential gradient in the z-direction is large enough to add significant vertical perturbations at high latitude region, tilting the circular orbits that would otherwise stay on a plane parallel to the MW mid-plane. Therefore, we expect that the deviation is significant for stars at  $60^\circ < |b| < 80^\circ$  in the Solar vicinity.

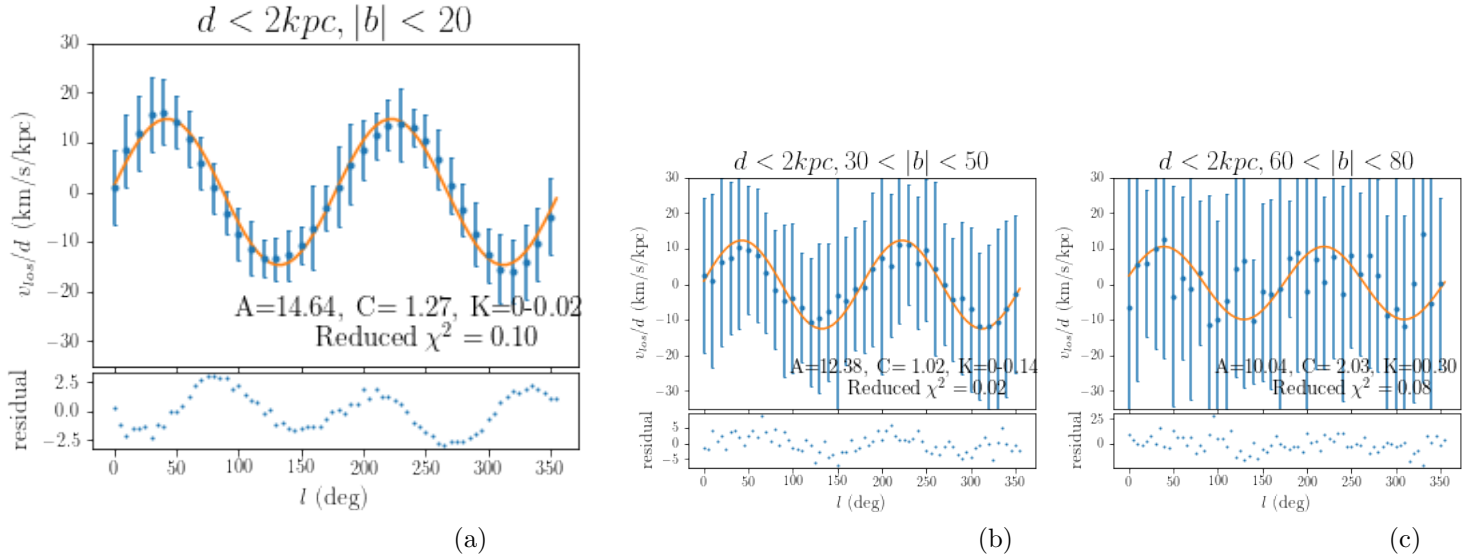


**Figure 12:** The function of binned median  $v_{los}/d$  over  $l$  for stars with  $d < 2\text{kpc}$  and (a)  $|b| \leq 20^\circ$ , (b)  $30^\circ < |b| < 50^\circ$ , and (c)  $60^\circ < |b| < 80^\circ$ .

### 3.1.4. Longitudinal profiles of $\mu_b$

For proper motion in the latitude direction,  $\mu_b$ , we expect to see more nonzero value at the middle  $|b|$  region because of the product  $\sin b \cos b$  in Eq12. In Fig 13,

different from  $\mu_l$  and  $v_{los}$  discussed above,  $\mu_b/\cos b \sin b$  of stars with  $d < 2\text{kpc}$  and  $30 < |b| < 50$  are much more dispersed. In Fig 15, taking binned medians gives the double sinusoidal curve expected from Eq 12. The binned standard deviations for these binned  $\mu_b$  medians range from 50-100 km/s/kpc, much larger than the variation of the binned medians across  $l$ , ( $\pm 25\text{km/s/kpc}$ ). Thus, error bars are not plotted in Fig 15 to better show the dependency of binned  $\mu_b/\cos b \sin b$  medians on  $l$ . At  $l = 0^\circ, 90^\circ, 180^\circ, 270^\circ$ ,  $\mu_b = 0$ . Stars are descending from the perspective of LSR from  $l = 0$  to  $90^\circ$  and from  $180$  to  $270^\circ$  while ascending from  $l = 90^\circ$  to  $180^\circ$  and from  $270^\circ$  to  $360^\circ$ .

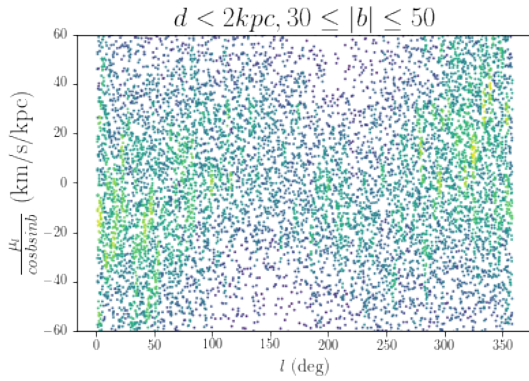


**Figure 13:** Longitudinal profiles of  $\mu_b/\cos b \sin b$  for stars with  $d < 2\text{kpc}$ ,  $30^\circ < |b| < 50^\circ$

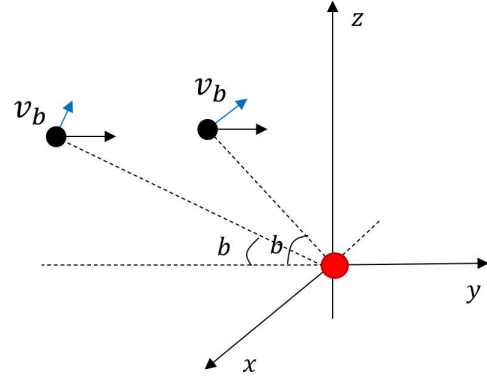


**Figure 14:** The change in latitude  $b$  and  $v_b$  with respect to the Sun for a star in a circular orbit at some latitude over the MW mid-plane. The absolute height of the star does not change because  $v_z = 0$ , but its galactic latitude changes as it approaches or moves away from the Sun.

Because the derivation of Oort constants assumes stars are close to the MW mid-plane and, thus, the discussion on  $\mu_l$  and  $v_{los}$  is more prevalent than the motion approaching or leaving the MW mid-plane. In fact,  $\mu_b$ , the proper motion in the latitudinal direction is also a kinematic tracer of the MW differential rotation. In Fig 14, let's look at a star at some vertical distance from the MW mid-plane and on a circular orbit with a constant  $v_\phi$  and  $v_z = 0$ .<sup>1</sup> As this star rotates around the GC at a different  $v_\phi$  than the Sun, its relative position with respect to the Sun changes, so it appear to approach or move away from the Sun while maintaining its absolute height. The angle between the line-of-sight and the horizontal plane parallel to the Milky Way mid plane, which is just the galactic latitude  $b$ , result a  $\sin b$  velocity component in

<sup>1</sup> Such an orbital configuration is not valid. We only use it for the purpose of demonstrating the connection between  $\mu_b$  and differential  $v_\phi$  around the Milky Way center.



the galactic latitude  $b$  direction perpendicular to the line-of-sight,  $v_b$ . As illustrated in Fig 14, this  $b$  angle varies when the star moves closer or away from the sun, so does  $v_b$ . Therefore,  $\mu_b = \frac{v_b}{d}$  is also a tracer for the stellar in-plane motion. Its dependency on  $l$  can be used to derive Oort constants and study the differential rotation of the Milky Way. This component,  $v_b$ , is larger for stars with higher  $b$  because of the  $\sin b$  component. Thus, in our simulation, we look at  $\mu_b$  of stars with mid range  $b$  values. However, for stars with very high  $|b|$ , that is away from the disc in the vertical direction, their orbits are rather non-circular due to the potential perturbation in the vertical direction. These stars tend to have larger vertical velocities, which can give a more dominant contribution to  $\mu_b$  than the effect coming from differential rotation discussed above.

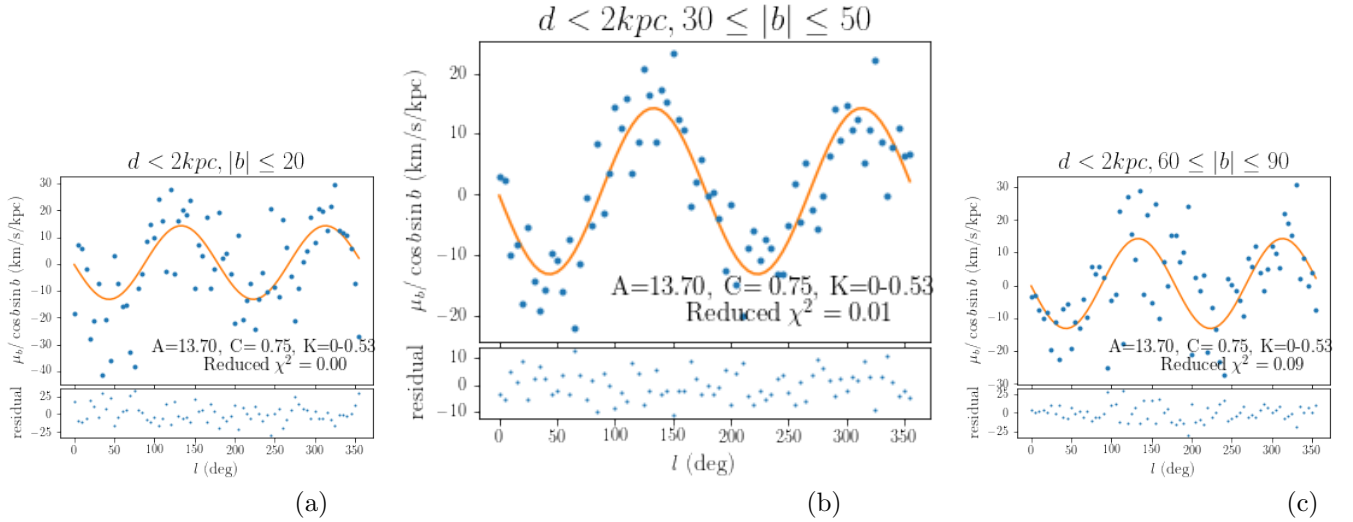


**Figure 15:** The function of binned median  $\mu_b / \cos b \sin b$  over  $l$  for stars with  $d < 2\text{kpc}$  and (a)  $|b| \leq 20^\circ$ , (b)  $30^\circ \leq |b| \leq 50^\circ$ , and (c)  $60^\circ \leq |b| \leq 90^\circ$

In Fig 15, compared to the stars closer to the MW disk ( $|b| < 20^\circ$ ) or those that are much farther away from the MW disk ( $|b| > 60^\circ$ ), stars with  $|b|$  between  $30^\circ$  and  $50^\circ$  yield the most noticeable double sinusoidal variation with  $l$ . In the residuals profiles, the residual for the group with  $30^\circ < |b| < 50^\circ$  distribute randomly over the smallest range compared to the other two groups. This suggests the group with  $30^\circ < |b| < 50^\circ$  gives the most satisfactory fit to the model predicted by Eq 12.

On the other hand, in Fig 16, for larger spatial coverage,  $d < 4\text{kpc}$ , binned median of  $\mu_b / \cos b \sin b$  shows a more evident double sinusoidal function than stars within  $2\text{kpc}$  and  $1\text{kpc}$ . The residual vs  $l$  panels suggests that the dispersion about the medians is the least when all the samples in a larger region around the Sun are included. This is likely because for a larger sample size, the binned medians are less subjective to any extreme individual values. However, the trade-off for including more samples is applying the first-order Taylor expansion in a much larger region than Sun vicinity.

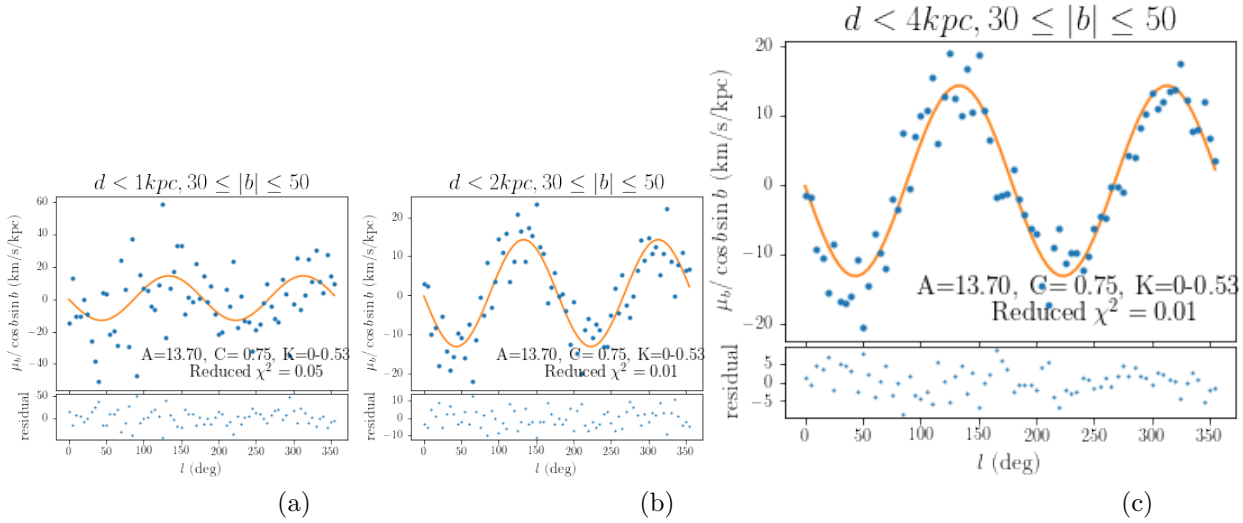


**Figure 16:** The function of binned median  $\mu_b / \cos b \sin b$  over  $l$  for stars with  $30^\circ \leq |b| \leq 50^\circ$  and (a)  $d \leq 1\text{kpc}$ , (b)  $d \leq 2\text{kpc}$ , and (c)  $d \leq 4\text{kpc}$ .

In Fig 16c, the first trough at  $l = 45^\circ$  is lower than the second one at  $l = 225^\circ$ . This suggests that the double sinusoidal function from the first-order Taylor expansion possibly under approximate higher order dependency proportional to  $\sin(3l)$ ,  $\sin(4l)$  and so on.

### 3.2. The effect of radial and vertical velocity profiles on $\mu_l$ , $v_{los}$ , $\mu_b$

In Appendix 22, we include the longitudinal profiles  $\mu_l / \cos b$ ,  $v_{los}/d$  and binned median of  $\mu_b / \cos b \sin b$  as a function of  $l$  under three different velocity profiles: 1)  $v_r$  and  $v_z$  2)  $v_r = 0$  and 3)  $v_z = 0$ . The result shows the spread in  $\mu_l$  is due to the variation of  $v_r$ . Both  $v_r$  and  $v_z$  have contributions to the scattering in  $v_{los}/d$ . When  $v_r$  is set to 0, the scattering around the central double sine curve is smaller as the brighter color indicates a higher density. Meanwhile, the contribution to the scattering in  $v_{los}/d$  by  $v_z$  is more significant. The difference of the binned median of  $\mu_b$  under three velocity profiles shows the deviations from the double sine function described by the Oort constants is attributed to the non-zero vertical velocity stars, agreeing well with the discussion in section 3.1.4.

### 3.3. Gaia DR2 observational data

#### 3.3.1. Gaia DR2: using the filtering criteria from literature

We now present results using Gaia DR2 data described in Section Method. In Fig 17, we show the  $\Delta\mu_l$  as a function of  $l$  in the region within  $d < 500\text{pc}$  and  $|b| < 20^\circ$  for stellar populations with  $G_{BP} - G_{RP} - E(BP_{RP}) < 0.8$ ,  $0.8 \sim 1$ ,  $1.2 \sim 1.6$ ,  $1.6 \sim 2.0$ ,  $2.0 \sim 2.4$  and  $\geq 2.4$ . The plots are not quite correct. At least for the first three stellar population based on color, the binned medians of  $\Delta\mu_l$  vs  $l$  fits Eq 11. The deviation from the double cosine function is larger for redder stellar populations as we

move across panel (a) to (d) in Fig 17. This is consistent with the fact that redder stars are kinematically older and reside in hotter thus less circular orbits. We also notice that there is a population of stars concentrated at  $l = 280^\circ$  and  $\mu_l$  around 20 km/s/kpc.

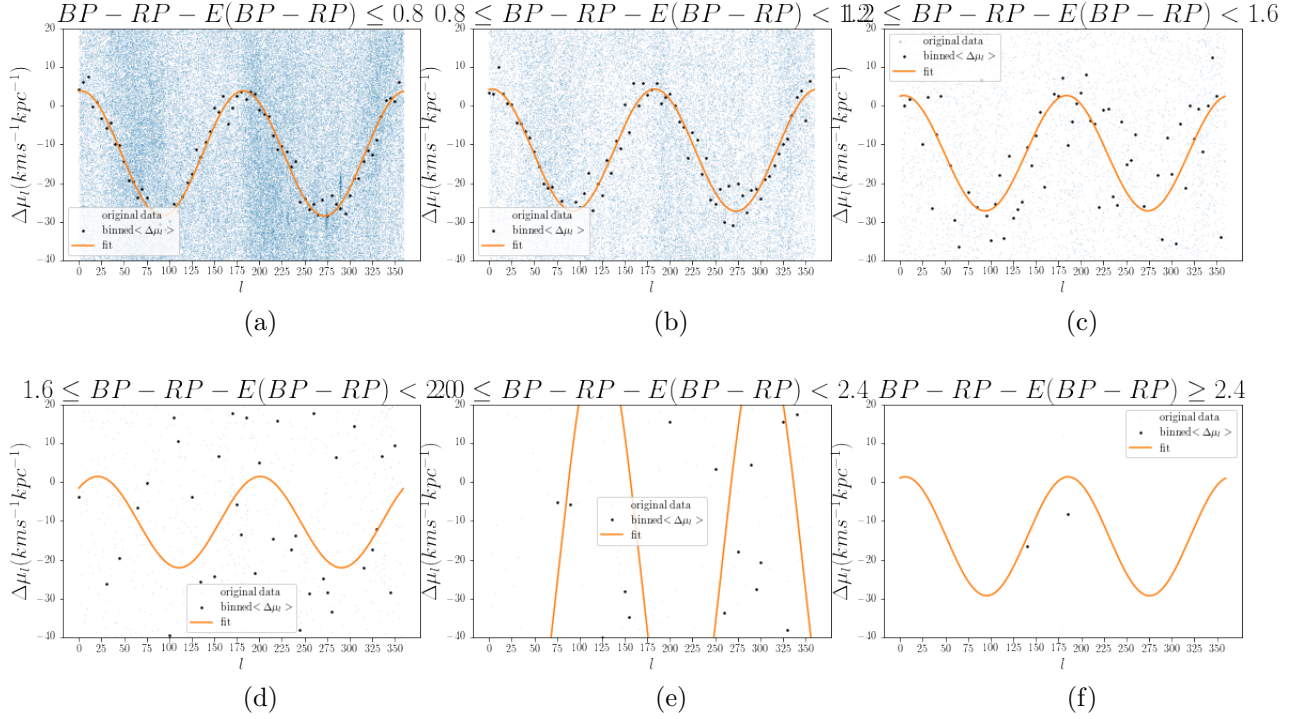


**Figure 17:**  $\Delta\mu_l$  as a function of  $l$  for stars with  $d < 500$  pc and  $|b| < 20^\circ$  divided into groups with  $G_{BP} - G_{RP} - E(BP - RP) < 0.8$ ,  $0.8 \sim 1.2$ ,  $1.2 \sim 1.6$ ,  $1.6 \sim 2.0$ ,  $2.0 \sim 2.4$  and  $\geq 2.4$ . **I really don't have the time to check what went wrong with these plots and add error bars. Forgive me, will do all of them this week**

Similar to  $\mu_l$ ,  $v_{los}$  for the two bluest stellar population calculated from the radial velocity data in DR2 are also well described by the double sine function predicted by the Oort constants (Fig 18). Despite radial velocity data entry is not available for all the stars in DR2, the two bluest stellar populations in Fig 18 show  $v_{los}$  can be used to derive the Oort constants. Table 2 shows the estimated peculiar motion ( $u_0, v_0, w_0$ ) from fitting  $\mu_l$  in Fig 17 by maximum likelihood estimation.  $v_{los}$  in Fig 18 is included into the log likelihood function for the three bluest stellar populations.

While the  $l$  dependencies of  $\mu_l$  and  $v_{los}$  for the stars in DR2 are consistent with the equations of the Oort constants,  $\mu_b$  for stars in the Solar vicinity and middle  $|b|$  range do not follow the curve predicted by Eq 12 as nicely as  $\mu_l$  and  $v_{los}$  do. Only for the bluest stellar population,  $\delta_{\mu_b}$  follows the double sinusoidal curve. This suggests that  $\mu_b$  is a less ideal tracer for deriving the Oort constants.

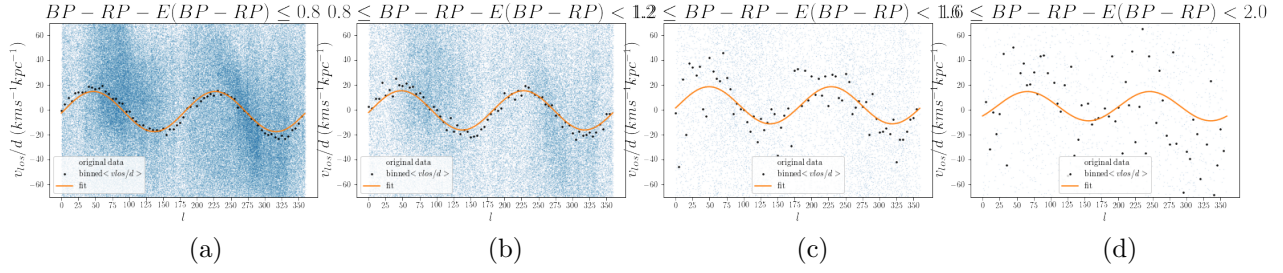


**Figure 18:**  $\Delta v_{los}$  as a function of  $l$  for stars with  $d < 500\text{pc}$  and  $|b| < 20^\circ$  divided into groups with  $G_{BP} - G_{RP} - E(BP - RP) < 0.8$ ,  $0.8 \sim 1, 2$ ,  $1.2 \sim 1.6$ , and  $1.6 \sim 2.0$ .

	$u_0(kms^{-1})$	$v_0(kms^{-1})$	$w_0(kms^{-1})$
$G_{BP} - G_{RP} - E(BP - RP) < 0.8$	10.85	19.44	7.07
$0.8 \leq G_{BP} - G_{RP} - E(BP - RP) < 1.2$	11.10	21.19	3.43??
$1.2 \leq G_{BP} - G_{RP} - E(BP - RP) < 1.6$	10.95	21.32	-45.15 ???
$1.6 \leq G_{BP} - G_{RP} - E(BP - RP) < 2.0$			
$2.0 \leq G_{BP} - G_{RP} - E(BP - RP) < 2.4$			
$G_{BP} - G_{RP} - E(BP - RP) \geq 2.4$			

**Table 2:** The value of solar peculiar motion ( $u_0, v_0, w_0$ ) from fitting  $\mu_l$  and  $v_{los}$  in Fig 17 and Fig 18 if available.

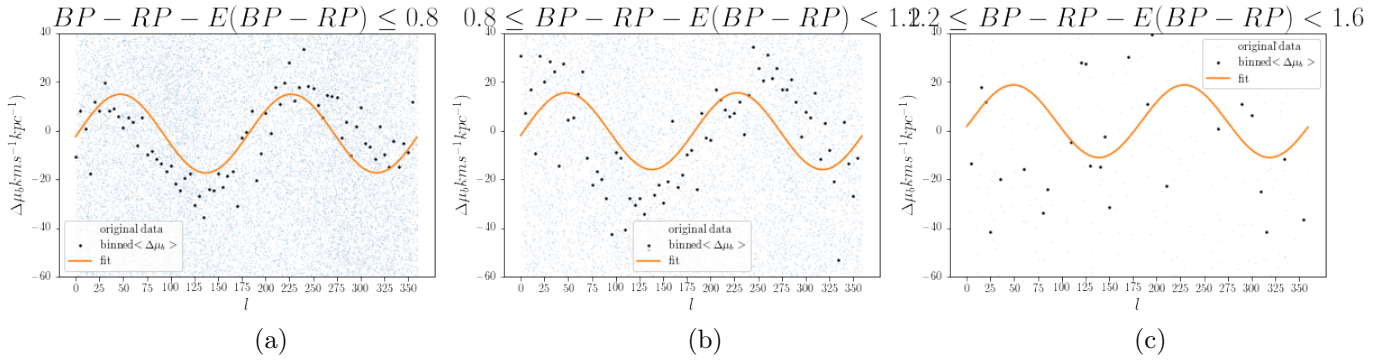


**Figure 19:**  $\Delta \mu_b$  as a function of  $l$  for stars with  $d < 500\text{pc}$  and  $40^\circ < |b| < 50^\circ$  divided into groups with  $G_{BP} - G_{RP} - E(BP - RP) < 0.8$ ,  $0.8 \sim 1, 2$ , and  $1.2 \sim 1.6$ .

Table 3 lists the values of the Oort Constants and their uncertainties estimated from the results in Fig 17, 18 and 19 using MCMC (See Appendix. X for the MCMC corner plot).

### 3.3.2. Applying filtering criteria based on Simulation to Gaia DR2

No result yet.

### 3.4. EDR3

: Have not decided if we should apply similar analysis to EDR3.

	$A(\text{km/s/kpc})$	$B(\text{km/s/kpc})$	$C(\text{km/s/kpc})$	$K(\text{km/s/kpc})$
$G_{BP} - G_{RP} - E(BP - RP) < 0.8$	16.09	-12.39	-1.19	-1.33
$0.8 \leq G_{BP} - G_{RP} - E(BP - RP) < 1.2$	15.65	-11.54	-1.73	-0.36
$1.2 \leq G_{BP} - G_{RP} - E(BP - RP) < 1.6$	14.73	-12.31	-2.14	3.72
$1.6 \leq G_{BP} - G_{RP} - E(BP - RP) < 2.0$				
$2.0 \leq G_{BP} - G_{RP} - E(BP - RP) < 2.4$				
$G_{BP} - G_{RP} - E(BP - RP) \geq 2.4$				

**Table 3:** The values of the Oort Constants and their uncertainties estimated from the results in Fig 17, 18 and 19 using MCMC.

#### 4. DISCUSSION AND CONCLUSION

Based on the comparison of the longitudinal profiles of  $\mu_l$  and  $v_{los}$  under different galactic distance and latitudinal restriction in the result section above, we chose  $d < 2\text{kpc}$  and  $|b| < 40^\circ$  as the sampling criteria in extracting the longitudinal profiles of  $\mu_l/\cos b$  and  $v_{los}/d$ . With MCMC, we determined the best-fitting parameters and their uncertainty:  $A = 14.84 \pm e1, B = -12.47 \pm e2, C = 1.27 \pm e3, K = 0.02 \pm e4$ , in the unit of km/s/kpc. (See Appendix XX for the corner map of the MCMC approximation)

Meanwhile, Gaia DR2 data of the two bluest stellar population,  $BP - RP - E(BP - RP) < 1.2$ , in 500pc from the Sun and less than  $20^\circ$  in the latitudinal direction yields the following measurement on  $A, B, C$  and  $D$ :

$$A = 15.93 \pm, B = -12.06 \pm, C = -1.30 \pm, K = -1.13 \pm \quad (17)$$

and the derived solar motion about LSR is:

$$u_0 = 10.97, v_0 = 20.24, w_0 = 8.65 \quad (18)$$

The measurements for A and B from simulation and our analysis on Gaia DR2 are in good agreement with those obtained in XX. The local gradient of the rotation curve is given by  $\frac{dv_\phi}{dR} = -(A + B)$ . According to our results from both simulation and Gaia DR2,  $-(A + B)$  is negative. It indicates the circular velocity decreases in Solar vicinity, which is in agreement with the rotation curve in Fig 1.

Recall in the Introduction, we mentioned that the mean offset value  $K$  describes the divergence in the local velocity field.  $K$  from simulation is not significantly different from 0, confirming that Milky Way simulated from quasi-isothermal distribution is axisymmetric. On the other hand, the non-zero mean offset derived from Gaia DR2 shows the motions in our actual Milky Way is non-axisymmetric.

comments on the solar peculiar motion derived in Table 2.

Our result with  $\mu_b$  from simulation and Gaia DR2 do not agree with Li et al. 2019. Why? I don't know. For Gaia DR2 data, the comparison of the  $v_\phi$  vs  $v_r$  phase plot between stars with  $|b| < 20^\circ$  and  $40^\circ < |b| < 50^\circ$  in Appendix Fig 23 shows that the radial velocities about the GC for the stars with  $40^\circ < |b| < 50^\circ$  distribute over a



larger non-zero range than the stars with  $|b| < 20^\circ$ . This suggests the stars we used to derive Oort constants from their proper motions in the latitudinal direction reside in less circular orbits. Because the assumption for Oort constants is circular orbital motion, more consideration is needed when using  $\mu_b$  to derive the Oort constants. In Section 3.2, we showed that  $\mu_b$  has strong double sinusoidal dependency on  $l$  as predicted by Eq 11 when the stars are in purely circular motions parallel to the MW mid-plane ( $v_{\perp 0}$  and  $v_z = 0$ ).

## REFERENCES

- Astropy Collaboration, Price-Whelan, A. M., SipHocz, B. M., et al. 2018, *aj*, 156, 123, doi: [10.3847/1538-3881/aabc4f](https://doi.org/10.3847/1538-3881/aabc4f)
- Binney, J. 2010, *MNRAS*, 401, 2318, doi: [10.1111/j.1365-2966.2009.15845.x](https://doi.org/10.1111/j.1365-2966.2009.15845.x)
- Binney, J., & Merrifield, M. 1998, *Galactic Astronomy*
- Bovy, J. 2015, *ApJS*, 216, 29, doi: [10.1088/0067-0049/216/2/29](https://doi.org/10.1088/0067-0049/216/2/29)
- . 2017, *MNRAS*, 468, L63, doi: [10.1093/mnrasl/slx027](https://doi.org/10.1093/mnrasl/slx027)
- Eilers, A.-C., Hogg, D. W., Rix, H.-W., & Ness, M. K. 2019, *ApJ*, 871, 120, doi: [10.3847/1538-4357/aaf648](https://doi.org/10.3847/1538-4357/aaf648)
- Feast, M., & Whitelock, P. 1997, *MNRAS*, 291, 683, doi: [10.1093/mnras/291.4.683](https://doi.org/10.1093/mnras/291.4.683)
- Foreman-Mackey, D., Hogg, D. W., Lang, D., & Goodman, J. 2013, *PASP*, 125, 306, doi: [10.1086/670067](https://doi.org/10.1086/670067)
- Gaia Collaboration, Brown, A. G. A., Vallenari, A., et al. 2020, arXiv e-prints, arXiv:2012.01533. <https://arxiv.org/abs/2012.01533>
- Gaia Collaboration, Prusti, T., de Bruijne, J. H. J., et al. 2016, *A&A*, 595, A1, doi: [10.1051/0004-6361/201629272](https://doi.org/10.1051/0004-6361/201629272)
- Gaia Collaboration, Brown, A. G. A., Vallenari, A., et al. 2018, *A&A*, 616, A1, doi: [10.1051/0004-6361/201833051](https://doi.org/10.1051/0004-6361/201833051)
- Green, G. 2018, *The Journal of Open Source Software*, 3, 695, doi: [10.21105/joss.00695](https://doi.org/10.21105/joss.00695)
- Joy, A. H. 1939, *ApJ*, 89, 356, doi: [10.1086/144060](https://doi.org/10.1086/144060)
- Kerr, F. J., & Lynden-Bell, D. 1986, *MNRAS*, 221, 1023, doi: [10.1093/mnras/221.4.1023](https://doi.org/10.1093/mnras/221.4.1023)
- Kuijken, K., & Tremaine, S. 1994, *ApJ*, 421, 178, doi: [10.1086/173635](https://doi.org/10.1086/173635)
- Levine, E. S., Heiles, C., & Blitz, L. 2008, *ApJ*, 679, 1288, doi: [10.1086/587444](https://doi.org/10.1086/587444)
- Li, C., Zhao, G., & Yang, C. 2019, *ApJ*, 872, 205, doi: [10.3847/1538-4357/ab0104](https://doi.org/10.3847/1538-4357/ab0104)
- Lin, C. C., Yuan, C., & Roberts, W. W., J. 1978, *A&A*, 69, 181
- Luri, X., Brown, A. G. A., Sarro, L. M., et al. 2018, *A&A*, 616, A9, doi: [10.1051/0004-6361/201832964](https://doi.org/10.1051/0004-6361/201832964)
- Metzger, M. R., Caldwell, J. A. R., & Schechter, P. L. 1998, *AJ*, 115, 635, doi: [10.1086/300198](https://doi.org/10.1086/300198)
- Mignard, F. 2000, *A&A*, 354, 522
- Mihos, C. unknown year, *The Solar Motion* nbsp;. <http://burro.case.edu/Academics/Astr222/Galaxy/Kinematics/solarmotion.html>
- Minchev, I., & Quillen, A. C. 2007, *MNRAS*, 377, 1163, doi: [10.1111/j.1365-2966.2007.11661.x](https://doi.org/10.1111/j.1365-2966.2007.11661.x)
- Mróz, P., Udalski, A., Skowron, D. M., et al. 2019, *ApJL*, 870, L10, doi: [10.3847/2041-8213/aaf73f](https://doi.org/10.3847/2041-8213/aaf73f)
- Ogrodnikoff, K. 1932, *ZA*, 4, 190
- Olling, R. P., & Dehnen, W. 2003, *ApJ*, 599, 275, doi: [10.1086/379278](https://doi.org/10.1086/379278)
- Olling, R. P., & Merrifield, M. R. 1998, *MNRAS*, 297, 943, doi: [10.1046/j.1365-8711.1998.01577.x](https://doi.org/10.1046/j.1365-8711.1998.01577.x)
- Oort, J. H. 1927, *BAN*, 3, 275
- Sellwood, J. A., & Carlberg, R. G. 2014, *ApJ*, 785, 137, doi: [10.1088/0004-637X/785/2/137](https://doi.org/10.1088/0004-637X/785/2/137)



- Siebert, A., Famaey, B., Minchev, I.,  
et al. 2011, MNRAS, 412, 2026,  
doi: [10.1111/j.1365-2966.2010.18037.x](https://doi.org/10.1111/j.1365-2966.2010.18037.x)
- Sofue, Y., & Rubin, V. 2001, ARA&A,  
39, 137,  
doi: [10.1146/annurev.astro.39.1.137](https://doi.org/10.1146/annurev.astro.39.1.137)
- Taylor, M. B. 2005, in Astronomical  
Society of the Pacific Conference Series,  
Vol. 347, Astronomical Data Analysis  
Software and Systems XIV, ed.  
P. Shopbell, M. Britton, & R. Ebert, 29
- Wegg, C., Gerhard, O., & Bieth, M. 2019,  
MNRAS, 485, 3296,  
doi: [10.1093/mnras/stz572](https://doi.org/10.1093/mnras/stz572)

## 5. APPENDIX

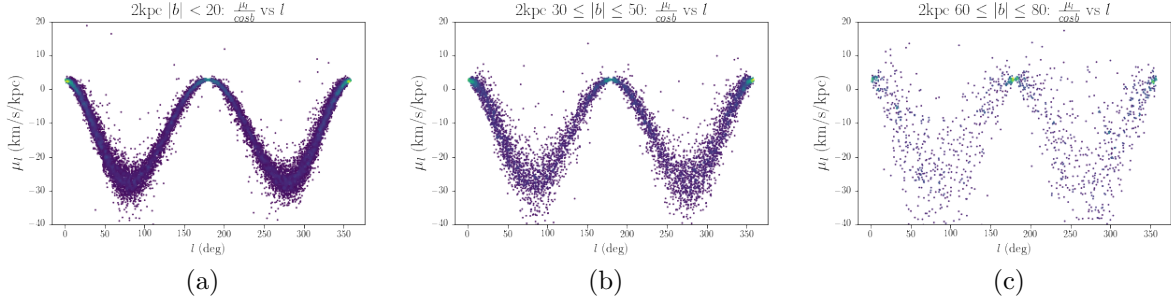


**Figure 20:** The distribution of  $\mu_l / \cos b$  over  $l$  for stars with  $d < 2\text{kpc}$  and (a)  $|b| < 20^\circ$ , (b)  $30^\circ \leq |b| \leq 50^\circ$ , and (c)  $60^\circ \leq |b| < 80^\circ$ .

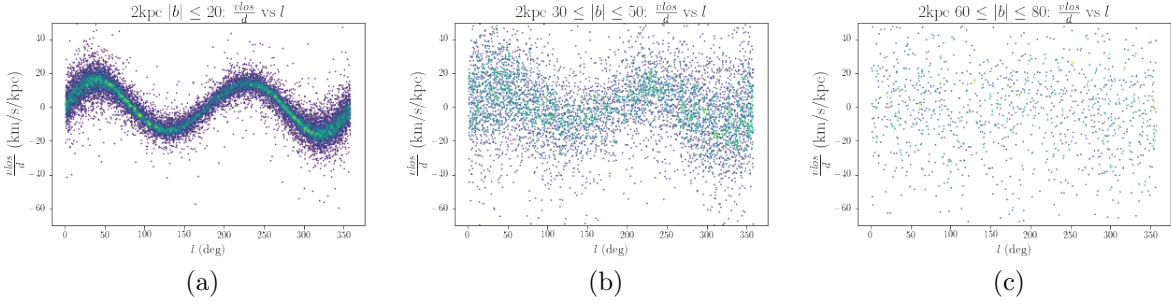


**Figure 21:** The distribution of  $v_{los} / d$  over  $l$  for stars with  $d < 2\text{kpc}$  and (a)  $|b| < 20^\circ$ , (b)  $30^\circ \leq |b| \leq 50^\circ$ , and (c)  $60^\circ \leq |b| < 80^\circ$ .

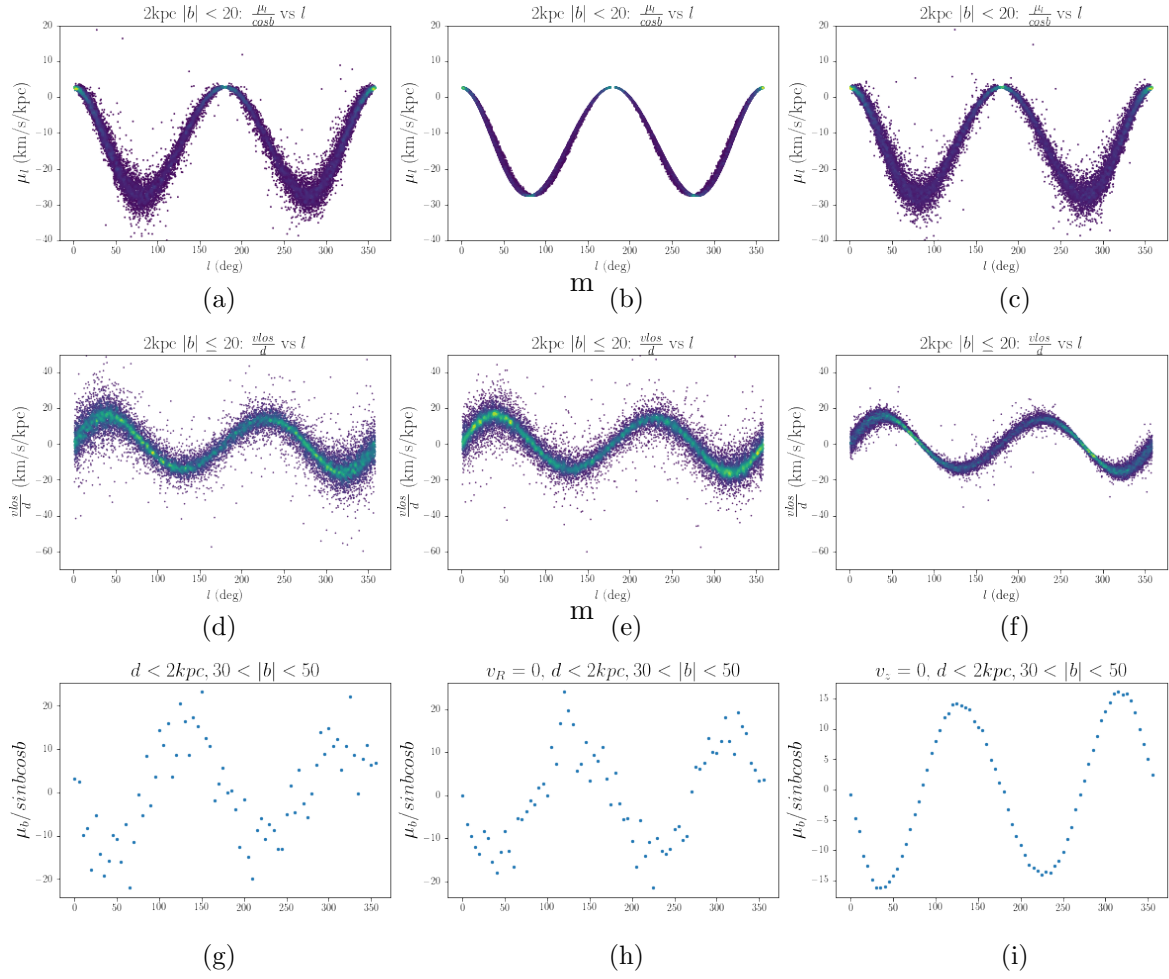


**Figure 22:**  $\mu_l/\cos b$ ,  $v_{los}/d$  and binned median of  $\mu_b$  as a function of  $l$  under three different velocity profiles from the leftmost to the rightmost columns: 1)  $v_r$  and  $v_z$  2)  $v_r = 0$  and 3)  $v_z = 0$ .

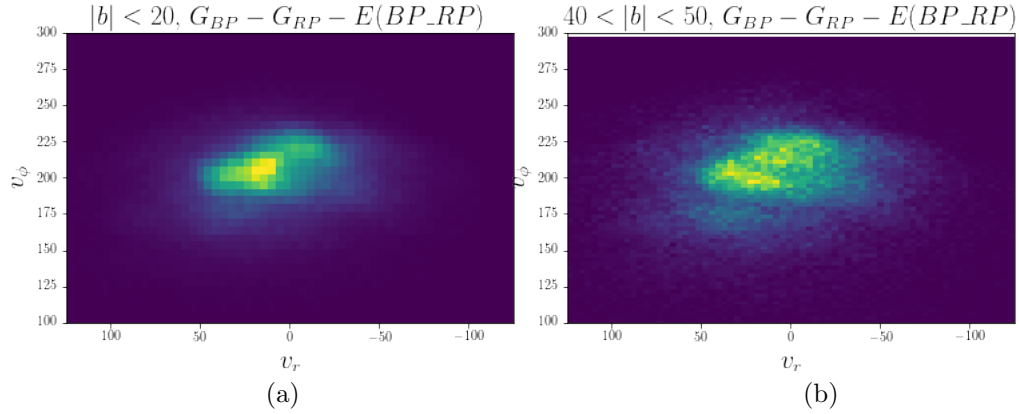


**Figure 23:**  $v_r$  VS  $v_\phi$  for stars at  $|b| < 20^\circ$  and  $40^\circ < |b| < 50^\circ$  within 500 pc from the Sun in Gaia Dr2. change the plot title to  $BP - RP - E(BP\_RP)$